Received: 25 December 2018 | Revised: 30 July 2019 | Accepted: 9 August 2019

DOI: 10.1111/ejn.14549

RESEARCH REPORT

EJN European Journal of Neuroscience FENS WILEY

Single-cell RNA-Seq characterization of anatomically identified OLM interneurons in different transgenic mouse lines

Jochen Winterer[1] | **David Lukacsovich**[1] | **Lin Que**[1] | **Andrea M. Sartori**[2] | **Wenshu Luo**[1] | **Csaba Földy**[1]

[1]Laboratory of Neural Connectivity, Brain Research Institute, Faculties of Medicine and Natural Sciences, University of Zürich, Zürich, Switzerland

[2]Institute for Regenerative Medicine, Department of Health Sciences and Technology, ETH Zürich, University of Zürich, Zürich, Switzerland

Correspondence
Csaba Földy, Brain Research Institute, University of Zürich, Winterthurerstrasse 190, 8057 Zürich, Switzerland.
Email: foldy@hifo.uzh.ch

Funding information
Schweizerischer Nationalfonds zur Förderung der Wissenschaftlichen Forschung, Grant/Award Number: 31003A_170085 and CRETP3_166815

The peer review history for this article is available at https ://publo ns.com/publon/10.1111/EJN.14549

Abstract

Inhibitory GABAergic interneurons create different brain activity patterns that correlate with behavioural states. In this characterizing study, we used single-cell RNA-Seq to analyse anatomically- and electrophysiologically identified hippocampal oriens-lacunosum moleculare (OLM) interneurons. OLMs express somatostatin (Sst), generate feedback inhibition and play important roles in theta oscillations and fear encoding. Although an anatomically- and biophysically homogenous population, OLMs presumably comprise of two functionally distinct types with different developmental origins, inferred from the expression pattern of serotonin type-3a (5-HT3a, or *Htr3a*) receptor subunit and 5-HT excitability in a set of OLMs. To broadly characterize OLM cells, we used the Sst-Cre and the BAC transgenic Htr3a-Cre mouse lines and separately analysed SstCre-OLM and Htr3aCre-OLM types. We found a surprisingly consistent expression of *Npy* in OLMs, which was previously not associated with the identity of this type. Our analyses furthermore revealed uniform expression of developmental origin-related genes, including transcription factors and neurexin isoforms, without providing support for the current view that OLMs may originate from multiple neurogenic zones. Together, we found that OLMs constitute a highly homogenous transcriptomic population. Finally, our results revealed surprisingly infrequent expression of *Htr3a* in only ~10% of OLMs and an apparently specific expression of the 5-HT3b subunit-coding gene *Htr3b* in Htr3aCre-OLMs, but not in SstCre-OLMs. However, additional in situ hybridization

Abbreviations: 5-HT3a, serotonin receptor type 3a; 5-HT3b, serotonin receptor type 3b; 5-HT, serotonin; AChRa4, nicotinic acetylcholine receptor a4; AP, action potential; BAC, bacterial artificial chromosome; CA1, cornu ammonis 1; Cck, cholecystokinin; CGE, caudal ganglionic eminence; FDR, false detection rate; Htr3a, serotonin receptor type 3a coding gene; Htr3b, serotonin receptor type 3b coding gene; HVG, high-variance genes; LOWESS, locally weighted scatterplot smoothing; mCPBG, 1-(3-chlorophenyl)biguanide; MGE, medial ganglionic eminence; Ndnf, neuron-derived neurotrophic factor; Npy (NPY), neuropeptide Y; OLM, oriens-lacunosum moleculare; PCA, principal component analysis; POA, preoptic area; Pvalb, parvalbumin; Reln, reelin; Sst, somatostatin; Vip, vasointestinal peptide.

Winterer and Lukacsovich authors contributed equally to this work.

Edited by Gianmaria Maccaferri.

experiments suggested that the differential expression of *Htr3b* may represent an unexpected consequence arising from the design of the Htr3a-Cre BAC transgenic line.

KEYWORDS

Htr3a, interneuron, neurexin, OLM, single-cell RNA-Seq

1 | INTRODUCTION

Oriens-lacunosum moleculare (OLM) interneurons represent a key inhibitory cell type class in the hippocampus and are involved in the generation of network oscillations (Gloveli et al., 2005; Klausberger & Somogyi, 2008; Maccaferri, 2005; Pangalos et al., 2013). OLMs receive cholinergic projections from the medial septum (Klausberger & Somogyi, 2008) and major excitatory drive from CA1 pyramidal cells (Böhm, Pangalos, Schmitz, & Winterer, 2015; Sylwestrak & Ghosh, 2012). The synaptic output of OLMs modulates activity of hippocampal ensembles by gating cortical inputs at distant dendrites of CA1 pyramidal cells (Leão et al., 2012; Royer et al., 2012), which is implicated in fear encoding (Lovett-Barron et al., 2014; Schmid et al., 2016; Siwani et al., 2018). Although OLMs form a morphologically and biophysically homogeneous population, they are presumed to originate from two neurogenic zones. Using mouse bacterial artificial chromosome (BAC) transgenic lines Nkx2.1-Cre, Htr3a-Cre and Htr3a-GFP and fluorescent reporter labelling in embryonic and adult mice, single OLM cells were shown to derive from either the medial or caudal ganglionic eminences (MGE and CGE, respectively; Chittajallu et al., 2013). Notably, these different OLM types displayed functionally distinct operations during network oscillations and only those of presumed CGE origin were excitable by application of the 5-HT3 receptor agonist mCPBG (hereafter referred to as 5-HT3-excitable OLMs). In contrast, OLMs of presumed MGE origin were insensitive to mCPBG (hereafter referred to as 5-HT3-insensitive OLMs). Nonetheless, a recent transcriptomic survey of GABAergic interneurons in the hippocampal CA1 revealed multiple cell populations, of which the identity of OLM cells was inferred by their expression of *Sst, Reln* and *Pnoc* and by the lack of *Npy* (Harris et al., 2018). Thus, OLMs were grouped as one population, regardless of their differences in 5-HT3 excitability, indicating that OLM cells originating from either CGE or MGE could not be distinguished by their transcriptomic profile.

While 5-HT excitability is presumed to be key for OLM cell function, the subunit composition of 5-HT3 receptors underlying 5-HT/mCPBG excitability remains unclear. Global genetic knockout of the 5-HT3a subunit interrupted fear extinction but did not affect fear encoding (Kondo, Nakamura, Ishida, Yamada, & Shimada, 2013). Although homomeric assembly of the 5-HT3a subunits was sufficient to form functional 5-HT3 receptor in heterologous expression systems (Maricq, Peterson, Brake, Myers, & Julius, 1991), its single-channel conductance was much smaller compared to those measured in native neurons (Hussy, Lukas, & Jones, 1994; Kelley, Dunlop, Kirkness, Lambert, & Peters, 2003). This observation led to the prediction that native 5-HT3 receptors were heteromeric. It was later proposed that 5-HT3a subunits may assemble with 5-HT3b (Davies et al., 1999) as well as nicotinic acetylcholine receptor a4 subunits (AChRa4; encoded by the *Chrna4* gene; Sudweeks, Hooft, & Yakel, 2002) to form 5-HT3 receptors.

To further investigate transcriptomic cell identity and composition of 5-HT3 receptors in OLM neurons, we performed electrophysiological patch-clamp recordings from morphologically identified OLM cells and collected their cytosolic mRNA for subsequent single-cell RNA sequencing. This approach offers straightforward access to the transcriptomic signature of OLM neurons, as cell type identification does not require clustering-based inferences and relies less on back-referencing to an existing knowledge base (Que, Winterer, & Földy, 2019).

We sampled OLM neurons from the Htr3a-Cre::Ai14 mouse line (hereafter denoted as 'Htr3aCre-OLMs'). Importantly, the Htr3a-Cre line, together with the Htr3a-GFP line, was generated using a BAC insert (same insert for both lines, GENSAT BAC address: RP24-377A21; Gerfen, Paletzki, & Heintz, 2013). As a result, these lines contain a second non-functioning BAC copy of the *Htr3a* gene, which drives Cre expression, and a fully functioning (BAC) copy of the *Htr3b* gene which is potentially capable of producing fully functional mRNA transcripts. While both lines are presumed to label cells with CGE origin (Akgül, Abebe, Yuan, Auville, & McBain, 2019; Chittajallu et al., 2013; Lee, Hjerling-Leffler, Zagha, Fishell, & Rudy, 2010), the Htr3a-Cre mouse line allows for labelling of all cells that actively express, or have expressed, *Htr3a*, whereas the Htr3a-GFP mouse line only labels cells that actively express *Htr3a* (Chittajallu et al., 2013; Lee et al., 2010). As it was recently shown that transcriptionally defined OLM cells did not express *Htr3a* mRNA (Harris et al., 2018), indicating transient expression of *Htr3a*, the Htr3a-GFP line would not allow the broad characterization of Htr3a-OLMs

we aimed for. To complement OLM cells of presumed CGE origin, we performed the same experiments in OLM cells sampled from the Sst-Cre::Ai14 mouse line (hereafter denoted as 'SstCre-OLMs'), as Sst^+-expressing cells are associated with MGE-derived neurons (Fogarty et al., 2007). Earlier studies have made use of the Nkx2.1 transgenic mouse line to identify OLMs originating from the MGE (Chittajallu et al., 2013). However, labelled cells in this line also include $Pvalb^+$ horizontal basket cells, which display similar dendritic arborizations and elongated cell bodies (Maccaferri, 2005). To circumvent this confounding factor, we chose to use the Sst-Cre line over the Nkx2.1 mouse line.

Our results confirmed infrequent, but not lacking, *Htr3a* expression in OLM cells. Furthermore, single-cell RNA-Seq analyses revealed that 5-Ht3b and AChRa4 subunit-coding genes were expressed in Htr3aCre-OLMs, independent of *Htr3a* expression, but virtually absent in SstCre-OLMs. In this manner, our results suggest that heteromeric 5-HT3 receptors possibly assemble from 5-HT3a, 5-HT3b and AChRa4 subunits and mediate 5-HT3 excitability in Htr3aCre-OLM neurons. Irrespectively, additional in situ hybridization revealed an atypical *Htr3b* expression in Htr3aCre-OLMs, possibly arising from the BAC copy of the *Htr3b* gene in this mouse line. In addition, we found expression of *Npy* in both cell types, which was further confirmed with immunostaining of recorded cells. This finding indicates that the expression of *Npy* is a characteristic feature of mouse hippocampal OLM neurons. Finally, the single-cell RNA-Seq analysis performed in this study disclosed new information on the developmental identity of OLM neurons. Specifically, we found that all OLMs, both Htr3aCre- and SstCre-types, expressed MGE-associated transcription factor and neurexin profiles. This indicates that these interneurons may actually derive from one common neurogenic pool and does not support the current view of a dual origin of OLM neurons.

2 | METHODS

2.1 | Animals

All animal protocols and husbandry practices were approved by the Veterinary Office of Zürich Kanton. The University of Zurich animal facilities comply with all appropriate standards (cages, space per animal, temperature, light, humidity, food, water), and all cages were enriched with materials that allow the animals to exert their natural behaviour. Both males ($n = 15$) and females ($n = 9$) were used for all experiments. To our best knowledge, sex has no influence on the parameters analysed in this study. Animals were killed when they were 3–7 weeks old. The following lines were used in this study: 1. Htr3a-Cre: B6.FVB(Cg)-Tg(Htr3a-cre) NO152Gsat/Mmucd, RRID:MMRRC_037089-UCD; 2. Sst-Cre: Sst<tm2.1(cre)Zjh>/J(#013044); and 3. Ai14: B6.Cg-Gt(ROSA)26Sor<tm14(CAG-tdTomato)Hze>/J Stock No: 007914. Together, we used 24 animals for this study: 12 animals (eight males and four females) from the Sst-Cre::Ai14 line and 12 animals (seven males and five females) from the Htr3a-Cre::Ai14 line.

2.2 | Electrophysiology

Horizontal slices from the medial part of the hippocampus (300 μm thick) were prepared from 3- to 4-week-old mice and incubated at 33°C in sucrose-containing artificial cerebrospinal fluid (sucrose-ACSF) (85 mM NaCl, 75 mM sucrose, 2.5 mM KCl, 25 mM glucose, 1.25 mM NaH_2PO_4, 4 mM $MgCl_2$, 0.5 mM $CaCl_2$ and 24 mM $NaHCO_3$) for 1 h and then held at room temperature until recording. Cells were visualized by infrared differential interference contrast optics in an upright microscope (Olympus; BX-51WI) using Hamamatsu ORCA-Flash 4.0 CMOS camera. Recordings were performed using borosilicate glass pipettes with filament (Harvard Apparatus; GC150F-10; o.d., 1.5 mm; i.d., 0.86 mm; 10 cm length) at 33°C in ACSF (126 mM NaCl, 2.5 mM KCl, 10 mM glucose, 1.25 mM NaH_2PO_4, 2 mM $MgCl_2$, 2 mM $CaCl_2$ and 26 mM $NaHCO_3$) with a standard intracellular solution (95 mM K-gluconate, 50 mM KCl, 10 mM HEPES, 4 mM Mg-ATP, 0.5 mM Na-GTP, 10 mM phosphocreatine and 2% biocytin; pH 7.2, KOH-adjusted, 300 mOsm). All recordings were made using MultiClamp 700B Amplifier (Molecular Devices), and signals were filtered at 10 kHz (Bessel filter) and digitized (50 kHz) with a Digidata 1440A and pCLAMP 10 (Molecular Devices).

2.3 | Analysis of electrophysiological parameters

V resting: Resting membrane potential values were recorded after establishing whole-cell configuration. *Max AP firing*: Action potential (AP) spiking frequencies were measured in response to current injections (from −150 pA in 25 pA steps). In each cell, AP firing frequencies and corresponding current injection values were plotted and fit with a sigmoid function. The amplitude of the sigmoid fit was used to represent maximum AP firing. *Firing Threshold*: We fit 20–80% (amplitude) of the above sigmoid with a linear function. For each cell, the firing threshold was determined where the linear fit intersected the 'x' (current injection)-axis. *Attenuation*: The ratio of the first and last AP peak amplitudes at maximal AP firing frequency. *Sag potential*: The amplitude of sag potential was measured in response to −150 pA current injections and represents the difference in minimum membrane potential measured between 750 ms and 1,000 ms and median membrane potential between

1,500 ms and 2,250 ms during the current injection. *AP properties:* We analysed single AP properties by averaging all time-aligned APs from an individual trace that contained at least 3 APs. These averaged APs were fit with three linear regressions in three separate time intervals: (i) baseline fit before AP, (ii) ascending (20–80%) phase of AP and (iii) during the descending phase of AP (80–20%). In addition, we determined AP peak (max) and trough (min) times and voltage amplitudes. Using these readouts, we determined *time from AP peak to trough*, *AP base width*, *AP half-width*, as well as *AP symmetry* (i.e. temporal position of peak between ascending and descending phases of AP). *Input resistance*: The input resistance was calculated from the resulting current amplitude at the steady-state response to a 5 mV voltage step. *Series resistance:* From the same voltage step used to determine the input resistance, we calculated the series resistance using the initial max current amplitude at the beginning of the voltage step. C*apacitance:* We determined the charge of the 5 mV voltage step (i.e. the area between the steady-state current response, input resistance and the initial current response series resistance), and divided the charge by the voltage to reveal the capacitance of the cell. *Spike Frequency Adaptation:* Using the spike times at maximum current injection, we calculated the instantaneous frequency versus spike number and fit this with locally weighted scatterplot smoothing (LOWESS) function. We used the difference between the first and last values over the first value as frequency adaptation.

2.4 | Cell type identification and collection

Using the Sst-Cre::Ai14 and Htr3a-Cre::Ai14 reporter lines, we recorded from cells that displayed horizontally elongated cell bodies and horizontally orientated dendrites in the stratum oriens of the hippocampal CA1, resembling OLM neurons. During recordings, which lasted for ~15 min, cells were filled with biocytin (Sigma-Aldrich, 2%) for subsequent reconstruction of OLM neurons. After collection of cytosol, brain slices were fixed in 4% paraformaldehyde (Sigma-Aldrich) overnight.

2.5 | Immunohistochemistry and neuroanatomy

After overnight fixation, slices were transferred into 30% sucrose in 0.1M PB solution for 1 hr on a shaker at room temperature. Then, the slices were re-sectioned into four to five 60-μm-thick slices. For immunohistochemistry, slices were first permeabilized and blocked in incubating medium (0.1M PB containing 5% normal goat serum and 0.2% Triton) for 1 hr at room temperature and then incubated at 4°C for overnight with primary antibodies. Next day, slices were rinsed in 0.1 M PB and incubated with secondary antibodies 4°C for overnight. Immunoreactions for neuropeptide Y (NPY) were carried out with rabbit antibody (Abcam ab30914 diluted 1:500). A secondary antibody conjugated to Alexa 488 (diluted 1:500; Invitrogen A-11008) raised against rabbit was used to detect the location of the primary antibodies; streptavidin was conjugated to Alexa 405 for biocytin (diluted 1:500; Invitrogen S-32351). Slices were mounted in VECTASHIELD (Vector Laboratories) for analysis. Image stacks of specimens were imaged on a Leica TCS SP2 confocal microscope (Leica Microsystems). Images were quantified using ImageJ software. DAB staining was done with VECTASTAIN ABC Kit (Vector Laboratories) either on re-sectioned slices after de-mounting or on 300-μm slices after overnight fixation. Cells were visualized with an upright bright-field microscope (Olympus; BX-51WI) and reconstructed with Neurolucida (MicroBrightField, Inc.). Together, we made patch-clamp recordings from 159 cells, of which only those cells were included in the analysis (46 cells), in which cDNA concentration after reverse transcription and amplification was higher than 0.1 ng/μl and DAB staining revealed axonal and dendritic arborization characteristic to OLM neurons.

2.6 | Morphological analyses

Sholl analysis was done on Neurolucida reconstructions to study the dendritic branching of all cells that were processed for single-cell RNA-Seq. Concentric shells were defined by increasing radii in 50-μm steps. Analysis of each shell was independent of the previous or following shell. The length (μm) was determined by the total length of all dendrites within each shell. The total amount of intersections within a shell was defined as the number of dendritic branches that crossed a given shell. Finally, all dendrite endings and the total amount of nodes (i.e. dendritic bifurcations) within a shell were determined.

2.7 | Next-generation single-cell RNA sequencing: sample collection

Methods and practices were identical as described in Földy et al., 2016. To minimize interference with subsequent molecular experiments, only a small amount of intracellular solution (~1 μl; not autoclaved or treated with RNase inhibitor) was used in the glass pipette for electrophysiological recordings. Before and during recording, all surface areas—including manipulators, microscope knobs and computer keyboard—that the experimenter needed to contact during experiments were cleaned with RNase AWAY solution (Molecular BioProducts). After whole-cell recording, the cytosol was aspired under visual guidance via the glass pipette used for recording, after which

the patch-clamp pipette was quickly removed from the cell and then from the amplifier head stage. The aspirate and intracellular solution in the patch-clamp pipette were then expelled into microtubes containing a cell collection buffer (provided with Clontech's RNA-Seq Kit, see below) using positive pressure while gently breaking tip of the glass pipette. Although the aspirated cytosol may have contained genomic DNA, our choice of cDNA preparation, which involved poly-A-based mRNA selection, virtually eliminates the possibility of genomic contamination in the RNA-Seq data. Cell collection microtubes were stored on ice until they were used.

2.8 | Next-generation single-cell RNA sequencing: cDNA library preparation

Same procedures were followed as described in Földy et al., 2016. Single-cell mRNA was processed using Clontech's SMARTer Ultra Low RNA Input v4 or SMART-Seq HT Kit. First, cells were collected via pipette aspiration into 1.1 µl of 10× collection buffer, spun briefly and snap frozen on dry ice. Samples were stored at −80°C until further processing, which was performed according to manufacturer's protocol. Resulting cDNA was harvested and analysed on the Fragment Analyzer (Advanced Analytical). Library preparation was performed using Nextera XT DNA Sample Preparation Kit (Illumina) as described in the manufacturer's protocol. cDNA concentration in single-cell samples ranged from 0.114 to 3.1949 ng/µl (median ± standard deviation: 0.638 ± 0.69 ng/µl), whereas the library concentration of the samples ranged from 0.4 to 4 nM (median ± standard deviation: 2.3 ± 1.0 nM). For controls, we performed RNA-Seq on samples that were collected from the extracellular space where no cell bodies were visible (note that mRNA collection from axonal or dendritic processes, which fill the extracellular space, cannot be fully excluded in these experiments; 'Extracellular aspiration'; $n = 5$; cDNA concentration ranged from 0.1236 to 0.5622; median ± standard deviation: 0.1494 ± 0.186 ng/µl). Following library preparation, cells were pooled and sequenced using NextSeq 300 high-output kit in an Illumina NextSeq 500 System with 2 × 150 paired-end reads.

2.9 | Bioinformatics: processing of RNA sequencing data

After sequencing, raw reads were de-multiplexed and pre-processed using Trimmomatic and Flexbar. Then, raw sequencing reads were aligned to the Ensembl GRCm38 reference transcriptome (Version-2015-06-25), using the STAR aligner with the following parameters: trimLeft = 10, minTailQuality = 15, minAverageQuality = 20 and minReadLength = 30, 'single-end/paired-end' and 'sense/antisense/both' options. Gene counts were calculated using HTSeq. For convenience, Ensembl gene IDs were converted to gene symbols using the mouse GRCm38 GTF file (ftp://ftp.ensembl.org/pub//release-86/gtf/mus_musculus/Mus_musculus.GRCm38.86.gtf.gz) as a reference. In the few cases where different Ensembl gene IDs identified the same gene symbol, average gene counts were used.

2.10 | Bioinformatics: quality control and normalization

All data analyses were performed using a combination of Python and R codes. For both quality control and normalization, we used scran (Lun, McCarthy, & Marioni, 2016). For each cell, we calculated the log of the number of unique genes that were detected, and removed cells with a value of at least 3.5 median absolute deviations (MAD) less than the median. For normalization, we used computeSumFactors with sizes of 10, 20 and 30. Cells that had negative or zero size were removed. Finally, for further analysis, gene counts were converted into log2 space with a pseudo-count of 1.

2.11 | Bioinformatics: selecting high-variance genes and dimension reduction

To detect high-variance genes (HVG), we started with genes that had an average log2-normalized expression higher than 0.1 (14,840 out of 22,800), and calculated the mean and variance of the expression of each gene. We fit these two variables using a locally weighted scatterplot smoothing (LOWESS) and estimated the technical component of the variance as the fitted curve and the biological component as the remainder. We fit a second LOWESS to the square of the biological component to get its variance. Using this variance, we selected as HVG those genes whose biological component was at least 1 and had a false detection rate (FDR) less than 5% (700 genes). We then used HVG to perform principal component analysis (PCA), a linear dimension reduction method.

2.12 | Bioinformatics: analysis of neurexin isoforms in single-cell RNA-Seq data

For each cell, we calculated canonical splice junction levels and averaged the results across Cre lines to get the mean and SEM. For each exon junction, we normalized the results so that the sum of splice-in and splice-out equalled to 1 (Figure 7b). For a regression fit, we plotted the normalized splice-in levels in SstCre-OLM versus Htr3aCre-OLM and fitted it with a linear regression 95% confidence interval. For more detailed description on this analysis, see Lukacsovich et al. (2019).

2.13 | In situ hybridization

Mice were anaesthetized and transcardially perfused with saline, followed by 4% paraformaldehyde solution (Electron Microscopy Sciences). Brains were removed and postfixed for 24 hr at 4°C. Afterwards, brains were (a) transferred to 30% sucrose in 0.1 M PB, pH 7.2, and stored at 4°C for 3 days for cryoprotection, (b) embedded in Tissue-Tek OCT compound and 3) frozen in 2-methylbutane (Sigma-Aldrich Chemie GmbH, Buchs, Switzerland) cooled to −40°C with liquid nitrogen and stored at −20°C until further processing. For in situ hybridization analysis, tissue blocks were cut horizontally into 14-µm-thin sections using cryostat, spread on glass slides and stored at −20°C until further processing. We used RNAscope probes against *Chrna4* (Probe-Ms-Chrna4 #429871; Advanced Cell Diagnosis) and *Htr3b* (Probe-Ms-Htr3b-C3 #497541-C3; Advanced Cell Diagnosis). Experimental protocols were according to manufacturer's protocol (Advanced Cell Diagnosis). Briefly, slides were thawed at room temperature for 15 min. Subsequently, slides were treated with ACD hydrogen peroxide for 10 min and washed twice in water for 2 min each, before incubation in ACD target retrieval buffer for 10 min at 98–100°C. Slides were washed first in water and then in 100% EtOH (Reuss Chemie, Taegerig, Switzerland), and then, protease treatment was applied for 30 min at 40°C in the ACD HybEZ™ oven. Subsequently, sections were incubated in a mix containing the two hybridization probes for 2 hr at 40°C. After washing the slides twice in ACD washing buffer, probes were amplified in a consecutive manner, with two washing steps in ACD washing buffer in-between each amplification step. Further amplification steps were performed with HRP detecting the specific channel of the different probes, always with washing steps with ACD washing buffer in-between. The signals were developed with TSA Plus Fluorescein and TSA Plus Cyanine 5 (TSA plus Fluorescein and Cy5, PerkinElmer) for the probe targeting *Chrna4* and *Htr3b*, respectively. After the development of the last probe, sections were washed twice in ACD washing buffer and counterstained with ACD DAPI for 45 s at room temperature. Slides were coverslipped using fluorescence mounting medium (Mowiol, Merck) and let dry overnight in the dark. Afterwards, they were stored at 4°C upon imaging. Fluorescent images were acquired using a SP2 confocal microscope (Leica). Target region was imaged using 20× objective lens (0.7 NA). Brightness and contrast of the images were adjusted for presentation using ImageJ. Only cells that displayed horizontally elongated cell bodies and horizontally orientated dendrites in the stratum oriens of the hippocampal CA1 were included in the analysis as presumed OLMs. Expression patterns were categorized as H (high expression) for 6 or more puncta, L (low expression) for 3–6 puncta, or no expression for <3 puncta on the soma of presumed OLMs.

3 | RESULTS

To generate comprehensive anatomical, electrophysiological and transcriptional data from OLM interneurons, we performed patch-clamp recordings from cells in the stratum oriens of the CA1 hippocampus, in brain slices prepared

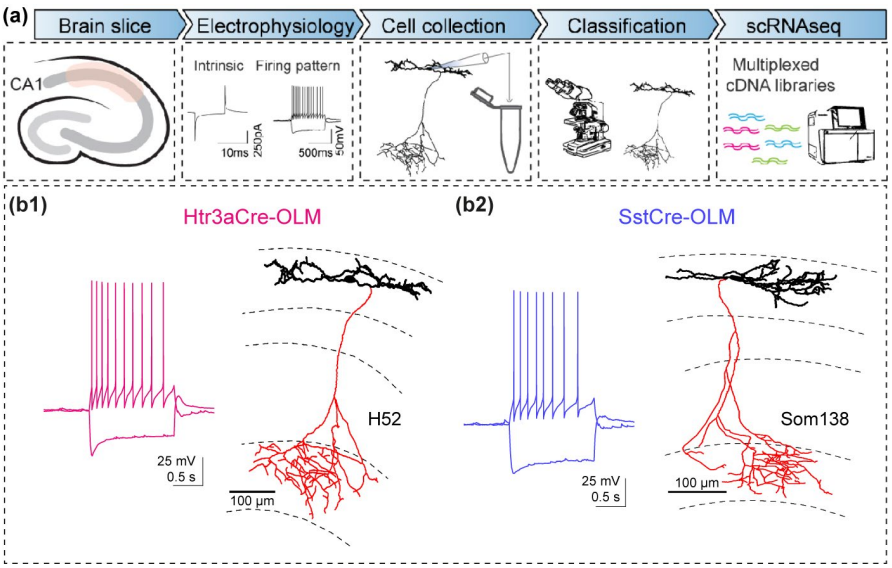

FIGURE 1 Combined anatomical, physiological and transcriptomic analysis of OLM interneurons. (a) In acute hippocampal brain slices, we identified OLM neurons based on tdTomato expression using the Htr3a-Cre::Ai14 and Sst-Cre::Ai14 transgenic lines. Single cells were electrophysiologically characterized, and their cytosolic mRNA was subsequently aspirated. Single-cell RNA sequencing was performed after confirming OLM identity by *post hoc* visualization of axons and dendrites. (b_1-b_2) Representative examples of Htr3aCre-OLM (cell ID 'H52') and SstCre-OLM neurons ('Som138'), respectively

from Htr3a-Cre::Ai14 and Sst-Cre::Ai14 mice, 3–4 weeks after birth. During patch-clamp recordings, we filled cells with biocytin, which allowed for post hoc morphological analysis, and aspirated their cytosol for subsequent RNA sequencing (Figure 1a; see also Földy et al., 2016). First, we morphologically characterized the recorded cells, and only proceeded with those for electrophysiological analysis and single-cell RNA sequencing which had axonal and/or dendritic morphology stereotypical to OLM cells (Figure 1b; see also Chittajallu et al., 2013; Böhm et al., 2015). In this manner, we analysed 23 Htr3aCre-OLM and 23 SstCre-OLM neurons.

3.1 | Anatomical profiling of OLM interneurons

First, we analysed the anatomical properties of OLM neurons. All cells that were included in the study were first reconstructed after DAB staining to identify the morphological characteristics of OLM cells, including the axonal projection to the lacunosum moleculare, the horizontally orientated soma and dendritic branching in the oriens (Figure 2a,b). These cells demonstrate that cytosol extraction for single-cell RNA-Seq did not interfere with morphological reconstruction. By contrast, brain slice preparation had a larger impact, because more distal parts of the 200- to 300-µm-long axon projections into the lacunosum moleculare were likely cut during slice preparation. For this reason, we quantified branching and length properties only of the dendrites, but not axons (Figure 2c). Sholl analysis revealed no difference between Htr3aCre-OLM or SstCre-OLM cells, regarding the total length, intersections, endings or nodes of the dendrites (Figure 2d).

3.2 | Electrophysiological profiling of OLM interneurons

In addition to morphological analyses, we quantified 12 electrophysiological parameters that relate to neuronal excitability (Figure 3a). These include both passive (e.g. input resistance and membrane capacitance) and active (e.g. properties of single AP and AP train firing) membrane properties sufficient to discern any potential difference between the Htr3aCre-OLM and SstCre-OLM cells. OLM interneurons are known to display a resting membrane potential (RMP) of approximately −65 mV that is intermediate to the more depolarized RMP of fast-spiking interneurons and the more hyperpolarized RMP of the neurogliaform family of hippocampal interneurons (Pelkey et al., 2017). Furthermore, OLM interneurons typically display a pronounced voltage sag in response to hyperpolarizing current injections. In addition, the spike frequency adaptation in these cells is considered to limit the maximum spiking frequency below the frequency typically observed in fast-spiking interneurons. We observed these typical features of OLM interneurons in both Htr3aCre-OLM and SstCre-OLM cells (sag potential: 0.51 ± 0.02 vs. 0.47± 0.03 mV; frequency adaptation ratio: 0.52 ± 0.03 vs. 0.43 ± 0.04; maximum AP firing: 53.2 ± 4.0 Hz vs. 62.2 ± 3.5 Hz; and RMP: −62.4 ± 1.2 vs. −63.4 ± 1.7, respectively). None of the parameters were significantly different; the lowest adjusted p-value (Student′s t test; $p = .84$) was in the case of the maximal AP firing rate (Figure 3b and Table 1). Taken together, and in agreement with previous findings (Chittajallu et al., 2013), we found that OLM neurons comprise a biophysically homogenous population because electrophysiological characterization of Htr3aCre-OLM and SstCre-OLM cells did not reveal differences.

3.3 | Transcriptomic profiling of OLM interneurons

To go beyond the anatomical and physiological characterization of OLM neurons, we next analysed the cell's complete transcriptomic profile using single-cell RNA-Seq. First, we evaluated RNA-Seq quality control parameters, which were not different between the Htr3aCre-OLM and SstCre-OLM cells, suggesting that expression levels of single genes between the two groups can be directly compared (Figure 4a and Table 2). Next, we examined the expression of marker genes that identify GABAergic cell types. Independent of the Cre line used for cell collection, we found consistent expression of GABA release-related *Gad1*, *Gad2* and *Slc6a1* in all OLM interneurons. By contrast, glutamate release-related vesicular glutamate transporter *Slc17a7* (detected in 2/46 cells) and *Slc17a6* (detected in 1/46 cells) genes were virtually not expressed across the whole population. Together,

FIGURE 2 Anatomical characterization of OLM interneurons. (a,b) Neurolucida reconstruction of all analysed Htr3aCre- (in a) and SstCre-OLM neurons (in b). The cell ID of each neuron is displayed next to the cell (Htr3aCre-OLM neurons are labelled as H#, and SstCre-OLM neurons are labelled as Som#). Each cell's dendrites and soma are shown in black, whereas the axon is shown in red. Scale bar is shown in panel a (bottom, right) and is applicable to every cell in panels a and b. In each drawing, cell layers are shown by dashed grey lines. The key for cell layers is shown in panel a (bottom, right) and is applicable to every drawing in panels a and b. (c) Sholl analysis of OLM dendritic segments. Two-dimensional projections of cells H53 and Som15 are shown as examples with overlaid concentric spheres (seen as circles). The radius of each sphere is shown in the right. (d) Dendritic length (Length, measured in three dimensions, d_1), number of dendrites intersecting a sphere (Intersections, d_2), number of dendrites ending in a spheric shell (Endings, d_3) and the number of dendritic branching points (Nodes, d_4) are shown. In each plot and spheric shell, data points represent single cells, and statistical data are overlaid as box plots

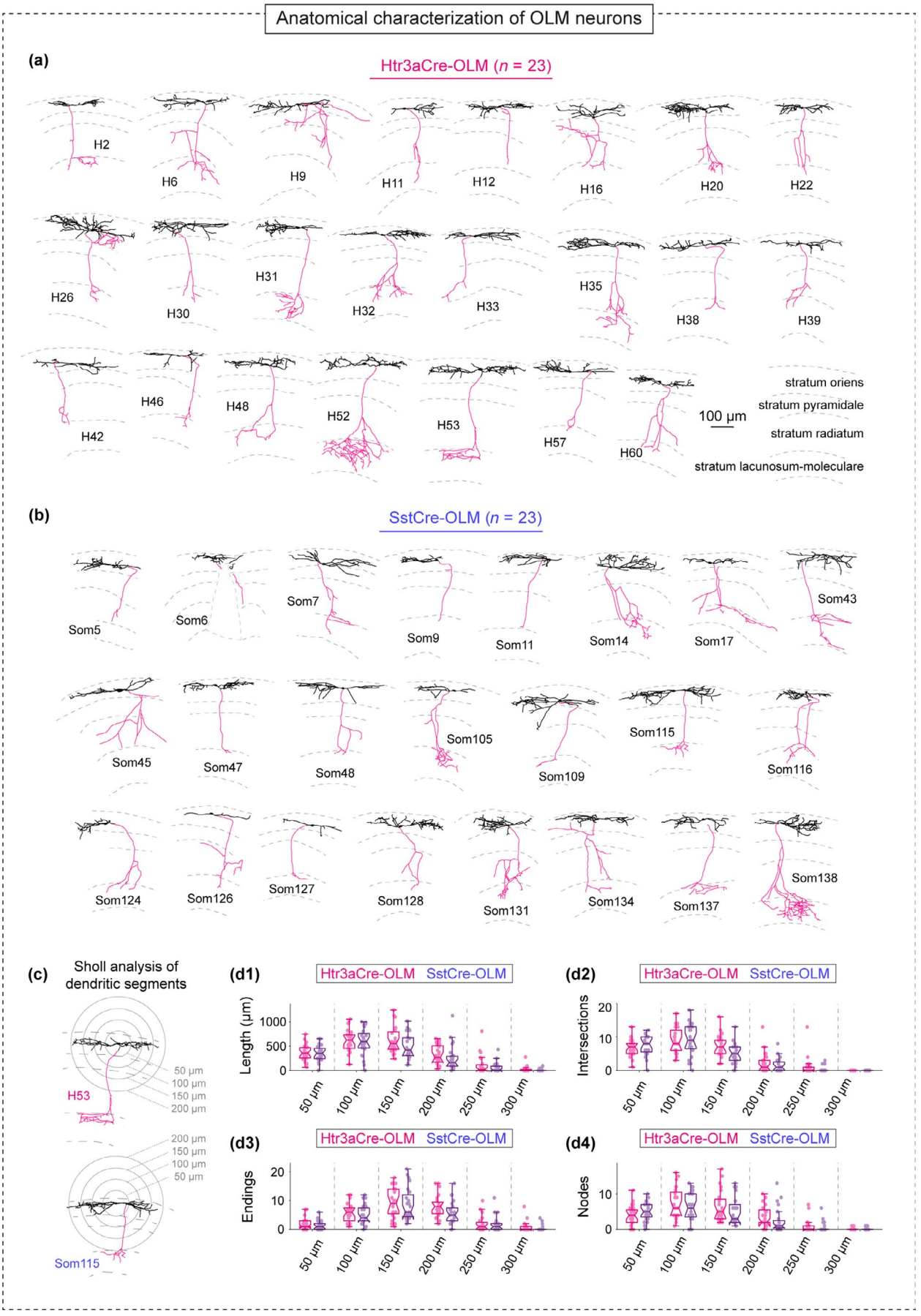
Anatomical characterization of OLM neurons
(a)
Htr3aCre-OLM (n = 23)
H2
H6
H9
H11
H12
H16
H20
H22
H26
H30
H31
H32
H33
H35
H38
H39
H42
H46
H48
H52
H53
H57
H60
100 µm
stratum oriens
stratum pyramidale
stratum radiatum
stratum lacunosum-moleculare
(b)
SstCre-OLM (n = 23)
Som5
Som6
Som7
Som9
Som11
Som14
Som17
Som43
Som45
Som47
Som48
Som105
Som109
Som115
Som116
Som124
Som126
Som127
Som128
Som131
Som134
Som137
Som138
(c)
Sholl analysis of dendritic segments
H53
50 µm
100 µm
150 µm
200 µm
Som115
200 µm
150 µm
100 µm
50 µm
(d1)
Htr3aCre-OLM SstCre-OLM
Length (µm)
1000
500
0
50 µm
100 µm
150 µm
200 µm
250 µm
300 µm
(d2)
Htr3aCre-OLM SstCre-OLM
Intersections
20
10
0
(d3)
Htr3aCre-OLM SstCre-OLM
Endings
(d4)
Htr3aCre-OLM SstCre-OLM
Nodes

the expression patterns of these genes confirmed GABAergic identity of the recorded cells (Figure 4b).

Second, we analysed the expression of a set of ion channels and synaptic markers that are associated with OLM identity, although not exclusively expressed (*Kcnc2, Kcnd3, Cacna1a, Cacna1g, Gria2, Gria4, Chrna2, Gabra1, Gabra2, Gabra5, Gabrg2, Syt1, Syt2, Elfn1* and *Grm1*). We found consistent expression of *Gria4*, *Kcnc2, Kcnd3, Cacna1a* and *Cacna1g*, which have been described to be present in OLMs (Lamsa, Heeroma, Somogyi, Rusakov, & Kullmann, 2007; Lien, Martina, Schultz, Ehmke, & Jonas, 2002; Pelkey et al., 2017; Topolnik, Chamberland, Pelletier, Ran, & Lacaille, 2009), as well as expression of *Chrna2,* which has been used as a marker for hippocampal OLM interneurons (Leão et al., 2012; Figure 4b). We also found consistent expression of *Gabra1* and *Gabrg2*, yet *Gabra5* was present in only 3/23 Htr3aCre-OLM and 0/23 SstCre-OLMs. This latter observation is consistent with the age-dependent remodelling of inhibitory synapses using this subunit, of which the function becomes dominant in adult animals (Magnin et al., 2019; Salesse, Mueller, Chamberland, & Topolnik, 2011), whereas this study was conducted in 3- to 4-week-old animals. Furthermore, we detected consistent expression of *Syt1* and lack of *Syt2*. This is in accordance with previous literature, as *Syt2* has been reported to be associated with $Pvalb^+$ cells (Chen, Arai, Satterfield, Young, & Jonas, 2017) and was shown to be absent in Sst^+ cells (Paul et al., 2017). In addition, we found both *Elfn1* and *Grm1* to be present throughout the cell population (Baude et al., 1993; Sylwestrak & Ghosh, 2012).

Third, we examined expression of interneuron subtype-specific markers, including calbindin and calretinin (*Calb1*, *Calb2*), cholecystokinin (*Cck*), neuron-derived neurotrophic factor (*Ndnf*), neuropeptide Y (*Npy*), parvalbumin (*Pvalb*), reelin (*Reln*), somatostatin (*Sst*), vasointestinal peptide (*Vip*) and prepronociceptin (*Pnoc,* Figure 4b). In agreement with previous studies, we found consistent expression of *Sst* and *Reln*, and sparse expression of *Pvalb* across both OLM neuron types (Harris et al., 2018; Pelkey et al., 2017). Of these, expression of the MGE-associated *Pvalb* in Htr3aCre-OLMs was surprising, because these cells were presumed to originate from CGE, and therefore should not be associated with *Pvalb* expression (Lee et al., 2010; Vucurovic et al., 2010). In addition, we detected *Pnoc* in both Htr3aCre-OLM (14/23) and SstCre-OLM (13/23), which was previously found to be present in OLM cells (Harris et al., 2018). Finally, we found consistent expression of *Npy* (Figure 4b,c). This observation was striking, because an earlier study showed the lack of NPY in OLM cells (0/4) in the rat hippocampus (Katona et al., 2014), and expression of its gene was previously used to exclude OLM identity in single-cell transcriptomic samples in mouse (Harris et al., 2018).

Fourth, we examined the expression of genes, which may mediate 5-HT excitability in OLM neurons: *Htr3a*, *Htr3b* and *Chrna4* (Figure 4b and d). Of these, we found infrequent expression of *Htr3a* in both Htr3aCre-OLM (5/23) and SstCre-OLM (2/23) types. While the lack of *Htr3a* expression in Htr3aCre-OLM cells may be counterintuitive, it suggests that most OLM cells collected from the Htr3aCre line (18/23) expressed this gene at an earlier time point, before cell collection, and also that some of the OLM cells collected from the SstCre line (2/23) presently expressed it at the time of collection. By contrast, *Htr3b* and *Chrna4* were more frequently expressed with an apparent bias towards the Htr3aCre-OLM cells (*Htr3b*: 11/23 Htr3aCre-OLM and 0/23 SstCre-OLM; *Chrna4*: 9/23 Htr3aCre-OLM and 3/23 SstCre-OLM cells).

Finally, we analysed expression of key developmental marker genes: including CGE-associated *Prox1*, *Htr3a* and *Sp8* (Akgül et al., 2019; Kessaris, Magno, Rubin, & Oliveira, 2014; Miyoshi et al., 2015, respectively), as well as MGE-associated

FIGURE 3 Electrophysiological characterization of OLM interneurons. (a) Electrophysiological parameters measured from patch-clamp recordings of OLM cells. (a_1) Schematic drawing shows a current transient in response to a voltage step that was used to quantify input resistance (applied voltage step divided by the measured steady-state current) and capacitance (measured charge divided by the applied voltage step) of cells, and series resistance of patch pipettes (applied voltage step divided by the measured peak capacitive current). (a_2) Example trace shows a cell's voltage response to hyperpolarizing and depolarizing current pulses that were used to quantify resting membrane potential (RMP), firing rate, attenuation and amplitude of the sag potential. (a_3) Analysis of action potential (AP) trains elicited by depolarizing current pulses. For each cell, AP firing frequencies in response to defined current injection pulses were quantified and fitted with a sigmoid curve. The amplitude of the sigmoid was used to extrapolate maximal firing rate, whereas a linear fit on the sigmoid curve's 20–80% segment was used to extrapolate firing threshold. (a_4) Time-averaged APs were used to determine peak AP amplitude, symmetry, base- and half-widths. (a_5) Drawing depicts linear fits that were used to determine peak AP amplitude, symmetry, base- and half-widths. First, the pre-AP baseline was fit with a linear function, which intersected the AP trace at inflection point 'a'. Then, a horizontal line ('A') was drawn through point 'a' to determine point 'b'. Second, the 20–80% between peak AP amplitude (determined as maximal value throughout the AP trace) and intersections 'a' and 'b' were separately fit with one-one linear function, characterizing the ascending and descending AP phase, respectively. The intersection point of these two linear fits was used to determine peak AP time. Third, a horizontal line ('B') was drawn through 50% of peak AP was used to determine points 'c' and 'd', which defined AP half-width. Finally, a vertical line ('C') though the peak AP time was used to determine point 'e' and its relative distance between points 'a' and 'b' that was used to define a value for AP symmetry. (b) Box plots depict measured electrophysiological parameters for Htr3aCre-OLM and SstCre-OLM interneurons. Each plot is labelled on the left, and data points represent single cells. Statistical significance (*p* values) using *t* test comparison is shown on top. None of the statistical comparisons were below 0.05

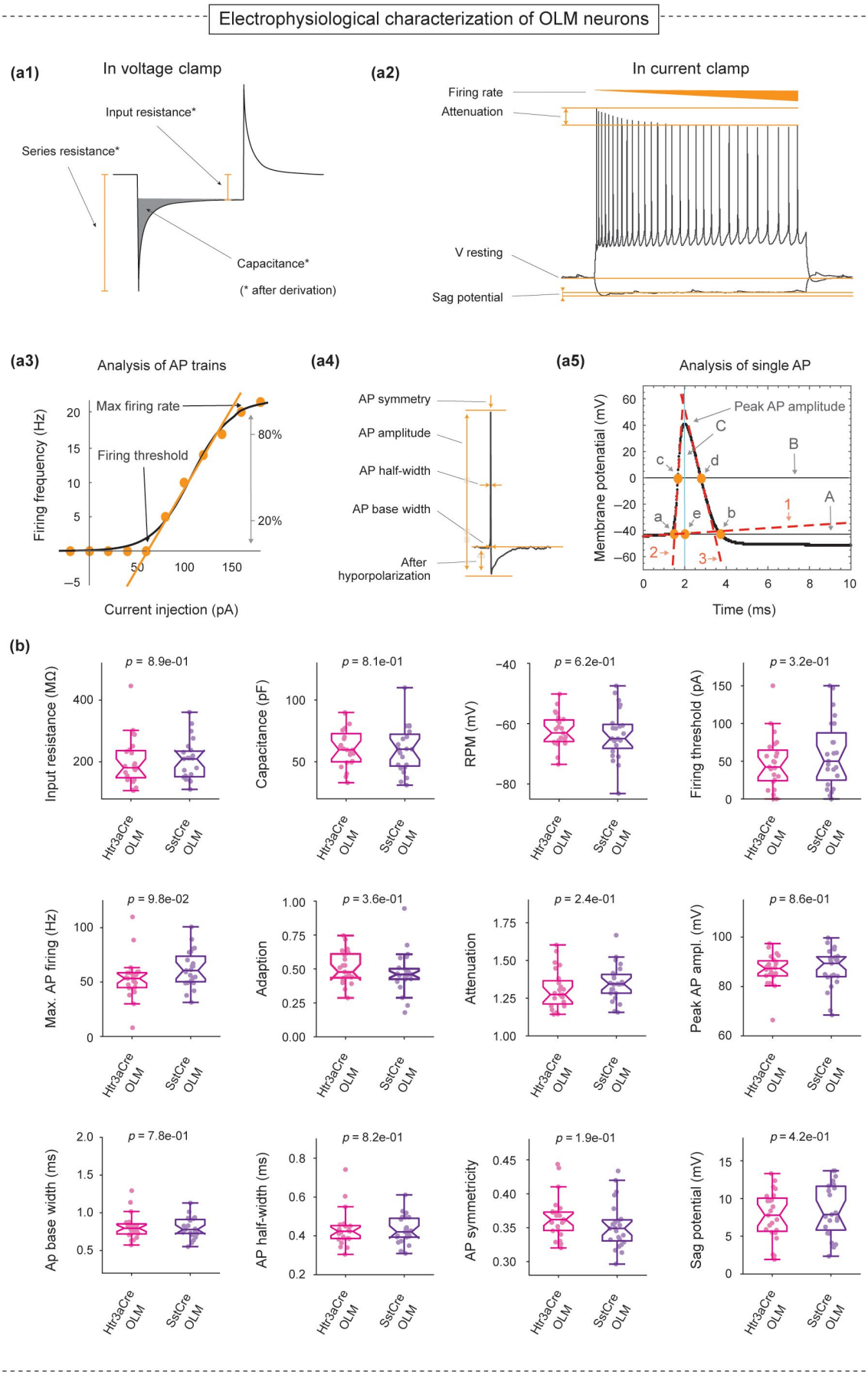
Electrophysiological characterization of OLM neurons
(a1)
In voltage clamp
Input resistance*
Series resistance*
Capacitance*
(* after derivation)
(a2)
In current clamp
Firing rate
Attenuation
V resting
Sag potential
(a3)
Analysis of AP trains
Max firing rate
Firing threshold
80%
20%
Firing frequency (Hz)
Current injection (pA)
(a4)
AP symmetry
AP amplitude
AP half-width
AP base width
After hyporpolarization
(a5)
Analysis of single AP
Peak AP amplitude
Membrane potenatial (mV)
Time (ms)
(b)
Input resistance (MΩ)
p = 8.9e-01
Capacitance (pF)
p = 8.1e-01
RPM (mV)
p = 6.2e-01
Firing threshold (pA)
p = 3.2e-01
Max. AP firing (Hz)
p = 9.8e-02
Adaption
p = 3.6e-01
Attenuation
p = 2.4e-01
Peak AP ampl. (mV)
p = 8.6e-01
Ap base width (ms)
p = 7.8e-01
AP half-width (ms)
p = 8.2e-01
AP symmetricity
p = 1.9e-01
Sag potential (mV)
p = 4.2e-01
Htr3aCre OLM
SstCre OLM

TABLE 1 Electrophysiological properties of OLM interneurons

	Htr3aCre-OLM	SstCre-OLM	Test	*p* value	*p* adjusted
Input resistance (MΩ)	201.35 ± 16.26	204.16 ± 13.57	*t* test	.8949	.8949
Capacitance (pF)	61.35 ± 3.23	60.13 ± 3.86	*t* test	.8093	.8949
RPM (mV)	-62.38 ± 1.15	-63.43 ± 1.73	*t* test	.6164	.8949
Firing threshold (pA)	47.41 ± 7.41	59.46 ± 9.32	*t* test	.3171	.8440
Max. AP firing (Hz)	53.22 ± 3.98	62.20 ± 3.52	*t* test	.0983	.8440
Adaptation	0.51 ± 0.02	0.47 ± 0.03	*t* test	.3553	.8440
Attenuation	1.31 ± 0.03	1.35 ± 0.02	*t* test	.2438	.8440
Peak AP amplitude (mV)	86.74 ± 1.34	87.11 ± 1.68	*t* test	.8642	.8949
AP base width (ms)	0.81 ± 0.03	0.80 ± 0.03	*t* test	.7790	.8949
AP half-width (ms)	0.44 ± 0.02	0.43 ± 0.01	*t* test	.8244	.8949
AP symmetricity	0.37 ± 0.01	0.35 ± 0.01	*t* test	.1932	.8440
Sag potential (mV)	7.74 ± 0.67	8.55 ± 0.73	*t* test	.4220	.8440

Note: Summary table of intrinsic and active properties of Htr3aCre-OLM and SstCre-OLM interneurons. Included are the input resistance, capacitance, resting membrane potential (RPM), firing threshold, maximal action potential (AP) firing frequency (max. AP firing), adaptation, attenuation, peak AP amplitude, AP base width, AP half-width, AP symmetricity and sag potential. Represented data are mean ± SEM, statistical test used and the significance level (*p* value and adjusted *p* value).

Lhx6, *Satb1* and *Sox6* (Close et al., 2012; Denaxa et al., 2012; Liodis et al., 2007). Note that *Lhx6*, and *Satb1* and *Sox6* are linked through transcription downstream of *Nkx2.1* and that *Sst* expression in cortical interneurons is regulated by *Lhx6*-dependent expression of *Satb1* (Batista-Brito et al., 2009; Denaxa et al., 2012; Pelkey et al., 2017). We detected *Htr3a, Prox1 and Sp8* in 5, 1 and 1 out of 23 Htr3a-OLMs, respectively. By contrast, all Htr3aCre-OLM and SstCre-OLM neurons consistently expressed MGE-associated marker genes (Figure 4b and e). This finding was unexpected in the case of Htr3aCre-OLM cells, which were presumed to originate from CGE and express CGE-associated *Htr3a*, *Prox1* and *Sp8*. Additional regression analysis furthermore supported the strong correlation between developmental marker expression for SstCre-OLM and Htr3aCre-OLM types ($R = 0.99$; Figure 4f). These findings demonstrated that a select set of GABA release-related, interneuron subtype-specific and developmental marker gene profiles in Htr3aCre-OLM and SstCre-OLM cells is identical, and furthermore suggested that molecular and developmental identity of the two types was more overlapping than previously thought.

3.4 | Comparison to Harris' transcriptomic survey

To further validate the RNA expression levels of the collected OLM interneurons, we included relevant cell populations of a previously conducted transcriptomic survey for comparisons (Harris et al., 2018; GEO: GSE99888; Figure 5). Note that in this study, expression of *Npy* was used to exclude OLM identity, but our data revealed consistent expression of this gene in OLMs. Therefore, we included both *Npy*-negative and *Npy*-positive neurons in our comparison, which included both Sst (11 groups)- and Pvalb (7 groups)-expressing groups. In addition, we added two cell populations, Cck (13 groups) and Vip (2 groups), both thought to derive from the CGE (Kessaris et al., 2014; Tricoire et al., 2011). As expected, we found consistent expression of *Sst* in all Sst cell populations and low *Sst* expression in the other cell populations; *Pvalb* could be detected in most cell groups, but was highly expressed across all Pvalb groups. *Npy* could be detected in

FIGURE 4 Single-cell RNA-Seq profiling of OLM interneurons. (a) Single-cell RNA sequencing quality parameters for SstCre-OLM and Htr3aCre-OLM neurons. Violin plots show sequencing and alignment parameters, including counts for reads, aligned reads, mapped reads, alignment rate, mapping rates and gene count. Each plot is labelled on the left, and data points represent single cells. None of the sequencing parameters were statistically different between SstCre-OLM and Htr3aCre-OLM neurons (the lowest adjusted *p*-value was for the alignment rate, $p = .187$). (b) Heatmap shows single-cell (left) and averaged (right) expression of key marker genes in SstCre-OLM and Htr3aCre-OLM types. Each column represents a single cell, for which cell ID is shown in the top. Averaged values are shown on the right. Circle's colour represents normalized gene expression levels (left scale bar), and size represents the proportion of cells in which the gene was detected within the cell type (applicable only to averaged values on the right, right scale bar). (c) Violin plots show *Npy* (neuropeptide Y) expression in SstCre-OLM and Htr3aCre-OLM cells. (d) Violin plots show 5-HT3 subunit-coding gene *Htr3a*, *Htr3b* and *Chrna4* expression in Htr3aCre-OLM and SstCre-OLM cells. (e) Averaged expression level of MGE-associated developmental markers was significantly higher than expression of CGE-associated markers in both Htr3aCre-OLM and SstCre-OLM cells. (f) Regression analysis of CGE-associated *Htr3a*, *Prox1* and *Sp8* and MGE-associated *Lhx6*, *Satb1* and *Sox6* developmental markers reveals strong correlation between Htr3aCre-OLM and SstCre-OLM cells

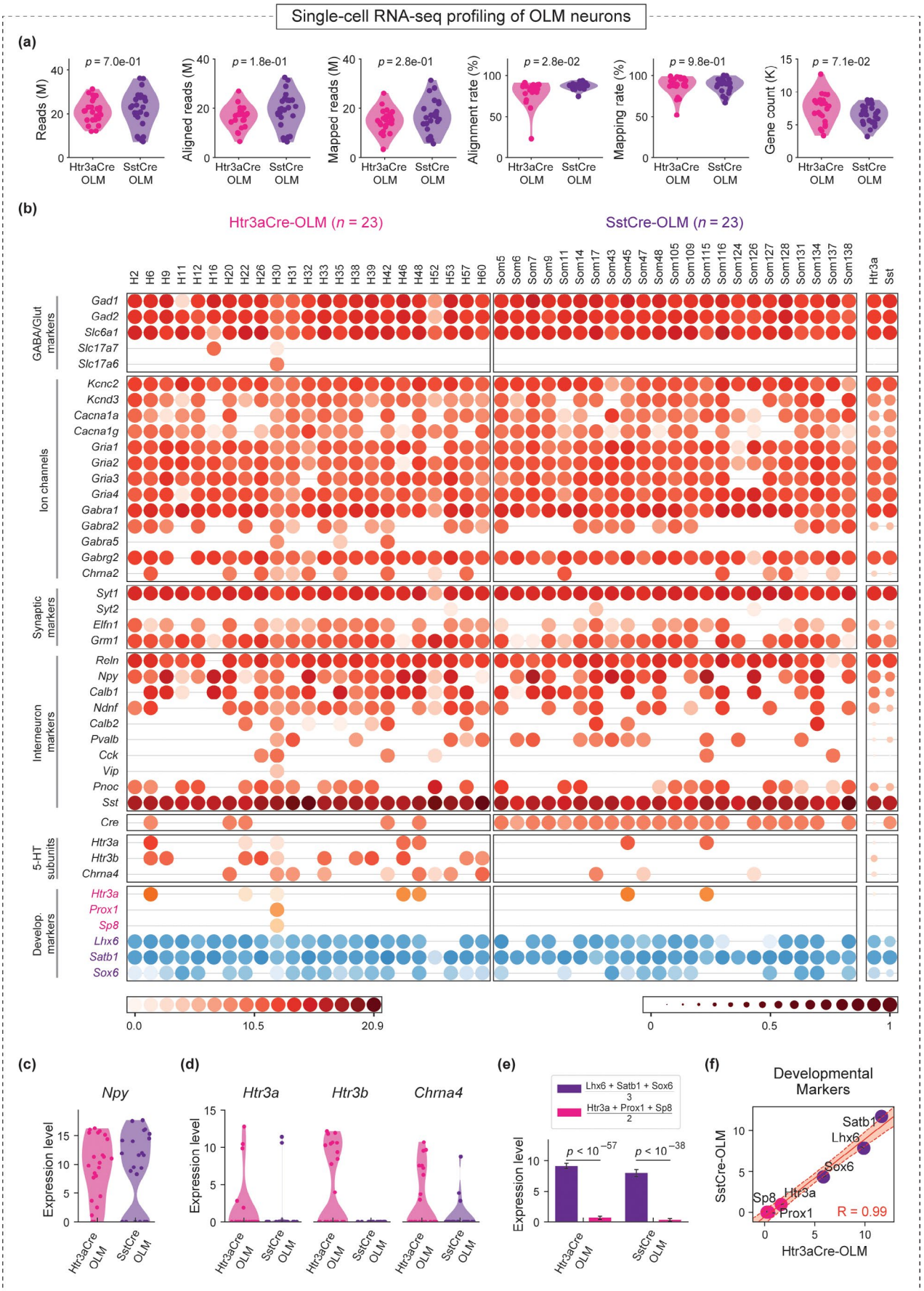
Single-cell RNA-seq profiling of OLM neurons
(a)
Reads (M)
p = 7.0e-01
Aligned reads (M)
p = 1.8e-01
Mapped reads (M)
p = 2.8e-01
Alignment rate (%)
p = 2.8e-02
Mapping rate (%)
p = 9.8e-01
Gene count (K)
p = 7.1e-02
Htr3aCre OLM
SstCre OLM
(b)
Htr3aCre-OLM (n = 23)
SstCre-OLM (n = 23)
H2 H6 H9 H11 H12 H16 H20 H22 H26 H30 H31 H32 H33 H35 H38 H39 H42 H46 H48 H52 H53 H57 H60
Som5 Som6 Som7 Som9 Som11 Som14 Som17 Som43 Som45 Som47 Som48 Som105 Som109 Som115 Som116 Som124 Som126 Som127 Som128 Som131 Som134 Som137 Som138
Htr3a Sst
GABA/Glut markers
Gad1 Gad2 Slc6a1 Slc17a7 Slc17a6
Ion channels
Kcnc2 Kcnd3 Cacna1a Cacna1g Gria1 Gria2 Gria3 Gria4 Gabra1 Gabra2 Gabra5 Gabrg2 Chrna2
Synaptic markers
Syt1 Syt2 Elfn1 Grm1
Interneuron markers
Reln Npy Calb1 Ndnf Calb2 Pvalb Cck Vip Pnoc Sst
Cre
5-HT subunits
Htr3a Htr3b Chrna4
Develop. markers
Htr3a Prox1 Sp8 Lhx6 Satb1 Sox6
0.0 10.5 20.9
0 0.5 1
(c)
Npy
Expression level
Htr3aCre OLM
SstCre OLM
(d)
Htr3a
Htr3b
Chrna4
(e)
Lhx6 + Satb1 + Sox6 / 3
Htr3a + Prox1 + Sp8 / 2
p < 10−57
p < 10−38
(f)
Developmental Markers
SstCre-OLM
Htr3aCre-OLM
Satb1
Lhx6
Sox6
Htr3a
Sp8
Prox1
R = 0.99

6/11 Sst, 2/7 Pvalb, 11/13 and 1/2 Vip-associated groups. Interestingly, we were unable to consistently detect RNA expression of 5-HT receptor subunits *Htr3a* and *Htr3b* in either Pvalb or Sst cell populations, in agreement with our own observations in OLMs identified from Sst-Cre but not Htr3a-Cre mice. Nonetheless, *Htr3a* was consistently expressed across Cck populations and in 1/2 of the Vip groups. Finally, we analysed expression of previous key developmental marker genes. We could not regularly detect CGE-associated markers *Htr3a*, *Prox1* and *Sp8* in either Sst or Pvalb populations, which were present in many Cck (11/13, 7/13, 11/13, respectively) and Vip (1/2, 2/2, 0/2, respectively) groups. Furthermore, MGE-associated markers *Lhx6*, *Satb1* and *Sox6* were expressed in most of the Sst and Pvalb populations, and absent in Cck and Vip groups, with the exception of low expression of *Satb1* (8/13 Cck and 1/2 Vip groups). Overall, these comparisons suggest strong similarities between our OLM cells and Harris et al.'s Sst cells, with exception of *Npy* expression.

In addition, we examined expression of presumed glial and astrocytic marker genes, which have recently been suggested to be contaminants in pipette-based as opposed to fluorescence-activated cell sorting (FACS)-based single-cell RNA-Seq data (Tripathy et al., 2018). However, we found that such genes were expressed in the FACS-based Harris' data in an apparent cell-type-specific fashion (Figure 5) and only some of these genes were detected in extracellular aspiration samples (see Luo et al., 2019, and Methods on using extracellular controls). Together, these suggest that either putative glial and astrocytic markers genes are expressed in interneurons or both pipette- and FACS-based approaches are equally prone to some level of contamination from a selection of genes.

Based on our single-cell RNA-Seq analysis and further augmented by meta-analysis of a previous data set, we deduced three predictions about OLM neurons from these single-cell transcriptomic data: (a) OLM cells express *Npy*, (b) Htr3aCre-OLM cells express the 5-HT3 receptor subunits Htr3b, while SstCre-OLM cells and Sst interneurons (in Harris et al.'s data) do not, and (c) OLM neurons express MGE-associated marker genes.

3.5 | NPY expression in OLM interneurons

First, we tested the prediction that NPY (peptide product of the *Npy* gene) may be present in OLM neurons. To confirm this, we made new patch-clamp recordings from OLM cells in the Htr3a-Cre::Ai14 transgenic mice (choice of this mouse line was arbitrary). During recordings, these cells were filled with biocytin (which, after DAB conversion, was used to morphologically confirm OLM identity) and subsequently immunostained for NPY. In this manner, we were able to confirm the presence of NPY in 3 out of 5 OLM neurons (Figure 6). Based on this observation, our data suggest that the expression of *Npy* mRNA is a characteristic feature of mouse hippocampal OLM neurons (Figure 4), in which the presence of the NPY peptide could be further confirmed in more than half of the cells tested.

3.6 | 5-HT receptor subunit expression in OLM interneurons

Our analyses indicated that Htr3aCre-OLMs, but not SstCre-OLMs, express the 5-HT3 receptor subunits *Htr3b* and that *Chrna4* is more abundant in Htr3aCre-OLMs compared to SstCre-OLMs. To validate this, we conducted in situ hybridization (RNAscope) experiments on samples from both Sst-Cre::Ai14 and Htr3a-Cre::Ai14 animals and analysed presumed OLM cells (Figure 7). We found that *Htr3b* expression was apparent in both transgenic mouse lines. However, we observed an enriched expression pattern for *Htr3b* in the Htr3a-Cre transgenic line. Moreover, we found that the majority of single cells displayed high expression levels of *Htr3b,* whereas this high-level expression was absent in Sst-Cre transgenic mice. In the Htr3a-Cre::Ai14 line, $n = 3$ mice and 60 slices were analysed, in which $n = 62$ cells displayed high, H (59%), and $n = 18$ displayed low, L (17%), expression of *Htr3b* out of 105 tdTomato-expressing, presumed OLM cells that were residing in the stratum oriens (Figure 7e, see Methods for details on calculation). In comparison, in the Sst-Cre::Ai14 line, $n = 2$ mice and 39 slices were analysed, in which $n = 0$ cells displayed high, H (0%), and $n = 16$ displayed low, L (13%), expression of *Htr3b* out of 122 tdTomato-expressing,

TABLE 2 Single-cell RNA-Seq parameters in OLM interneurons

	Htr3aCre-OLM	SstCre-OLM	Test	*p* value	*p* adjusted
Reads (M)	21.12 ± 1.06	21.87 ± 1.63	*t* test	.7013	.8416
Aligned reads (M)	16.69 ± 0.86	18.95 ± 1.40	*t* test	.1758	.3515
Mapped reads (M)	14.94 ± 0.91	16.66 ± 1.29	*t* test	.2815	.4223
Alignment rate (%)	80.61 ± 2.81	87.10 ± 0.74	*t* test	.0341	.2044
Mapping rate (%)	88.47 ± 2.20	88.41 ± 1.66	*t* test	.9822	.9822
Gene count (K)	7.47 ± 0.43	6.54 ± 0.28	*t* test	.0741	.2222

Note: Summary table of sequencing parameters for Htr3aCre-OLM and SstCre-OLM interneurons. Included are counts for reads, aligned reads, mapped reads, alignment rate, mapping rate and gene count. Represented data are mean ± SEM, statistical test used and the significance level (*p* value and adjusted *p* value).

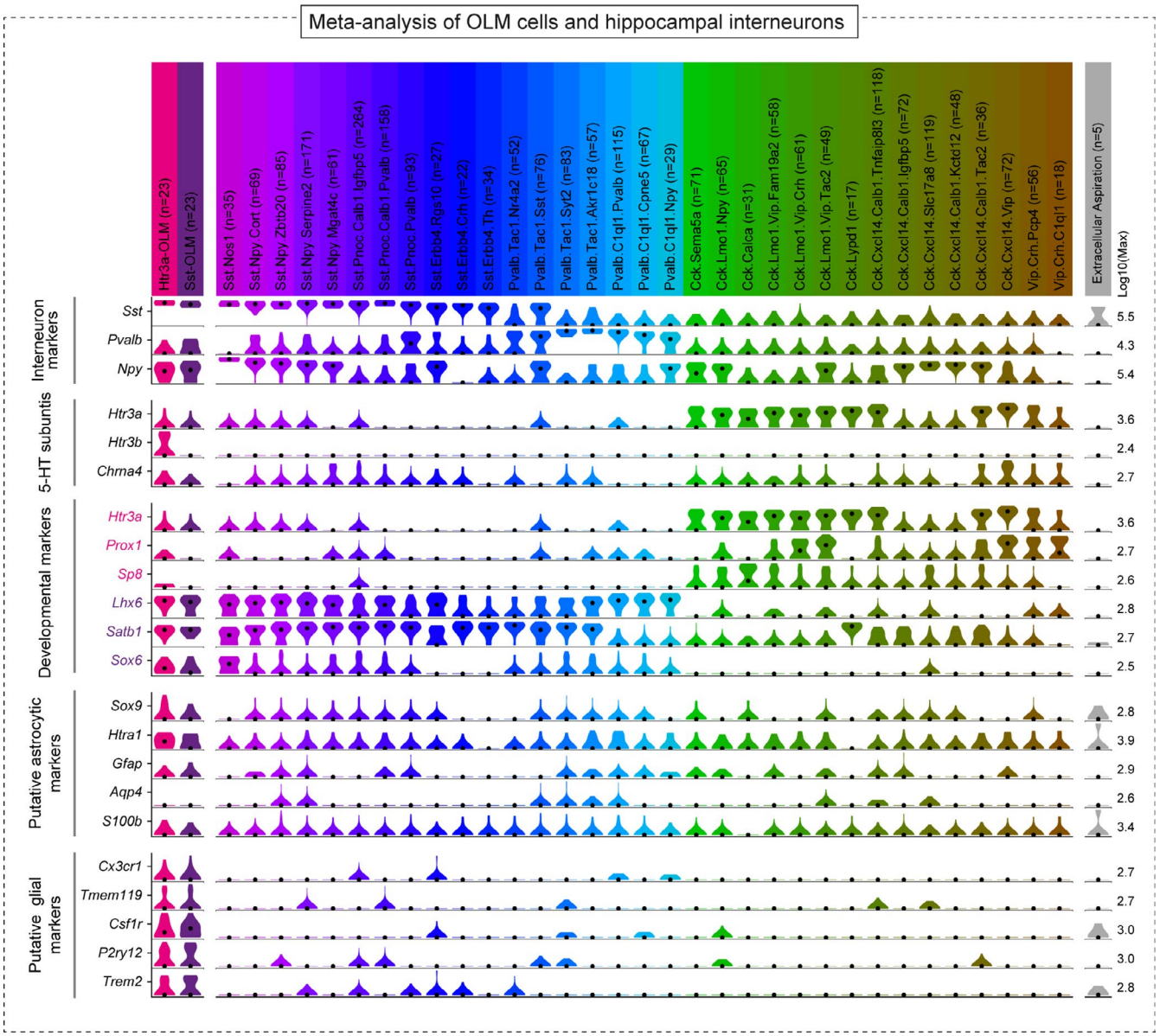

FIGURE 5 Meta-analysis of multiple transcriptomic cell populations. Violin plots show normalized gene expression levels for Htr3aCre-OLMs, SstCre-OLMs, cell populations of a recent transcriptional survey (Harris et al., 2018) as well as a control group of extracellular aspirations. Each column represents a single Sst, Pvalb, Cck, Vip or control group, and each row represents a single gene, grouped as interneuron markers, 5-HT3 receptor subunits, developmental, astrocytic and glial marker genes. The number of single cells included for each cell population is indicated in parentheses

presumed OLM cells (Figure 7e). Note that, beyond presumed OLMs, these patterns were observable in all cells residing in all layers of the hippocampus (in Htr3a-Cre::Ai14 line, $n = 198$ out of 708 tdTomato+ cells, or 28%, expressed high level of *Htr3b*; in comparison, in the Sst-Cre line, $n = 0$ out of 493 tdTomato+ cells, or 0%, were classified as high *Htr3b*-expressing cells; Figure 7f). In addition, in the Htr3a-Cre::Ai14, but not in the Sst-Cre::Ai14 line, we found 210 cells that highly expressed *Htr3b*, but not tdTomato, suggesting that *Htr3a* and *Htr3b* are independently regulated. Such enriched expression did not occur for *Chrna4*, which was expressed to a similar degree in both Htr3a-Cre and Sst-Cre samples (41% and 62% of tdTomato+ presumed OLM cells, respectively; Figure 7e). The detection of *Htr3b*-expressing OLMs using the Htr3a-Cre transgenic line was in accordance with our single-cell RNA-Seq data results (Figure 4). However, the complete absence of high *Htr3b*-expressing cells in Sst-Cre::Ai14 line was surprising, because such cells should have been detected in this transgenic line as well. Complementing this analysis, relevant in situ hybridization data in the Allen Mouse Brain Atlas also indicate lack of *Htr3b*-expressing cells throughout the hippocampus of wild-type animals (Lein et al., 2007; https://mouse.brain-map.org/gene/show/36293 and https://mouse.brain-map.org/experiment/show/74641318).

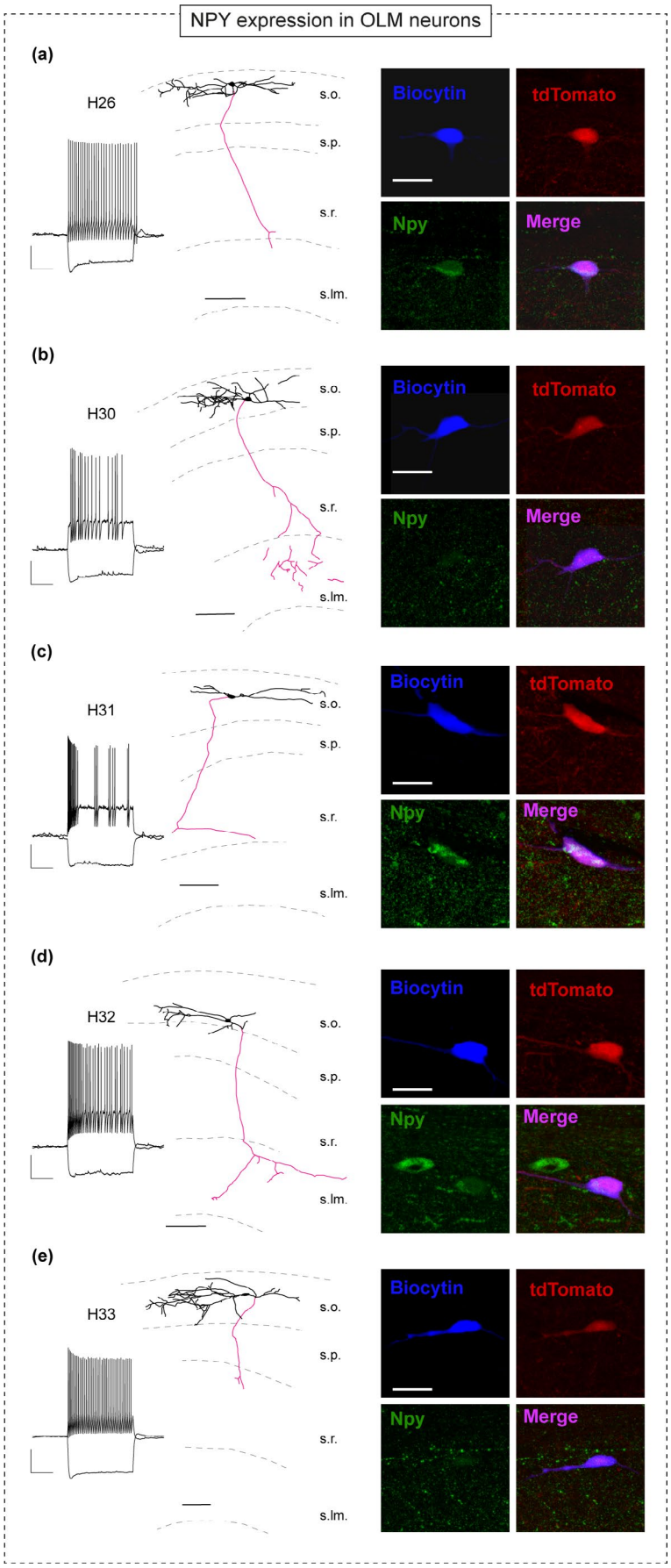

FIGURE 6 NPY peptide expression in OLM interneurons. (a–e) Electrophysiologically recorded and morphologically identified OLM neurons. During patch-clamp recordings, tdTomato+ cells were filled with biocytin, and after recordings, brain slices containing the recorded cells were fixed and re-sectioned into 60-μm-thick slices for immunochemical staining for biocytin and NPY. Left panels show morphological reconstructions after DAB conversion (scale bar: 100 μm), and inserts show the cells response to hyperpolarizing and depolarizing current pulses (horizontal scale: 0.5 s; vertical scale: 25 mV). Right panels show confocal images for biocytin, tdTomato, NPY and their merge (scale bar: 20 μm). OLM neurons in panels a, c and d were NPY+, whereas NPY content in OLMs in panels b and e could not be confirmed

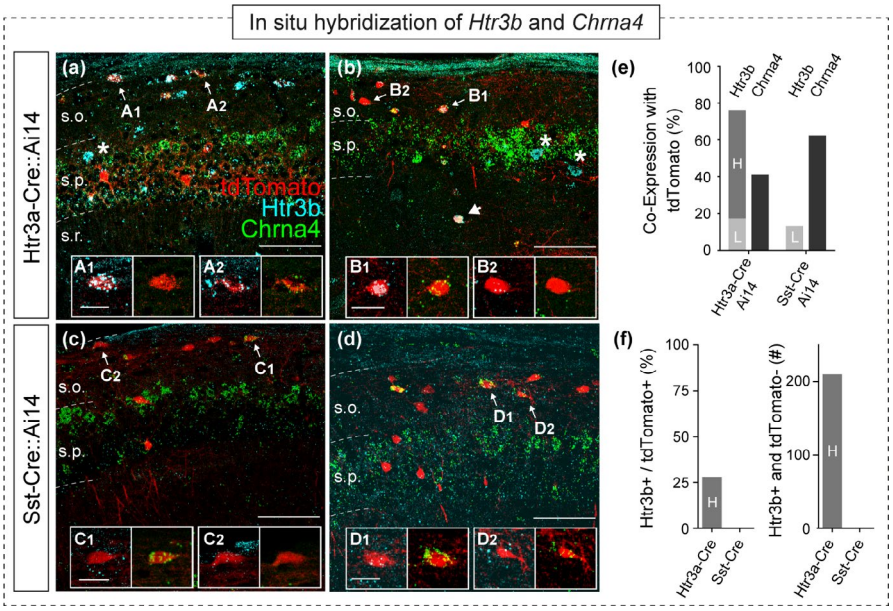

FIGURE 7 In situ hybridization of *Htr3b* and *Chrna4* in stratum oriens of hippocampal CA1. (a,b) Two confocal images show expression pattern of *Htr3a*/tdTomato (red), *Htr3b* (cyan) and *Chrna4* (green) in the BAC transgenic Htr3a-Cre::Ai14 mouse line (scale bar: 100 μm). Cells with high *Htr3b* but without tdTomato expression ('Htr3b+ and tdTomato-') are labelled with asterisks. Inserts a_1-a_2 and b_1-b_2 show higher magnification images of presumed OLM cells in a and b, respectively (scale bar: 25 μm). In each insert, left image shows *Htr3b* and right image shows *Chrna4* staining, overlaid on tdTomato. (c,d) Two confocal images show expression pattern of *Sst*/tdTomato (red), *Htr3b* (cyan) and *Chrna4* (green) in the Sst-Cre::Ai14 mouse line (scale bar: 100 μm). Inserts c_1-c_2 and d_1-d_2 show higher magnification images of presumed OLM cells in c and d, respectively (scale bar: 25 μm). In each insert, left image shows *Htr3b* and right image shows *Chrna4* staining, overlaid on tdTomato. (e) Bar graph shows the percentage of presumed OLM cells co-expressing *Htr3b* with tdTomato (grey for low expressing, L, and dark grey for high expressing, H) and *Chrna4* (black) in Htr3a-Cre::Ai14 and Sst-Cre:Ai14 mice. (f) Left bar graph shows the percentage of all hippocampal cells co-expressing *Htr3b* (H) with tdTomato in Htr3a-Cre::Ai14 and Sst-Cre::Ai14 mice. Right bar graph shows the total number of high *Htr3b*-expressing, but tdTomato-negative hippocampal cells

3.7 | Neurexin isoform expression in OLM interneurons

Contrary to the current view (Chittajallu et al., 2013), the expression of MGE-related, but lack of CGE-related, marker genes in both Htr3aCre- and SstCre-OLM neurons suggests that OLM neurons originate from the MGE. Recently, we have shown that the alternative splicing profile of neurexin-1 and neurexin-3, which are key presynaptic organizer cell adhesion molecules (Südhof, 2017), correlates extremely well with neurogenic origin and is distinct between cells that originate from the MGE versus CGE (Lukacsovich et al., 2019). Therefore, as a surrogate marker for developmental identity, we set out to examine neurexin isoform expression in OLM neurons. Neurexin-1 and neurexin-3 are encoded by *Nrxn1* and *Nrxn3*, respectively. Each gene has 6 canonical alternative splicing sites (ASS1-6; Figure 8a and c), in which the flanked exons are either retained (spliced-in) or excised (spliced-out) in a cell-type-specific manner (Südhof, 2017). Although the usage of ASS3 stands out as a characteristic difference between MGE and CGE cells (the flanked exon is uniformly spliced-in in MGE and spliced-out in CGE cells), the common behaviour of all *Nrnx1* and *Nrxn3* splice sites provides a more accurate proxy for developmental identity at the single-cell level. Therefore, we analysed alternative exon usage in all twelve *Nrxn1* (Figure 8b) and *Nrxn3* (Figure 8d) ASS-s. Because exon usage at these sites is independent (Lukacsovich et al., 2019; Schreiner et al., 2014; Treutlein, Gokce, Quake, & Südhof, 2014), we made pairwise comparisons at each ASS separately between the two OLM types. These analyses revealed no difference in the alternative splicing of neurexins between Htr3aCre-OLM and SstCre-OLM neurons (Figure 8b and d; Welch's *t* test, lowest *p*-value is for *Nrxn3* at ASS2-in, at $p = .878$). In addition, using information from all 12 ASS-s (see Methods for details on calculation), regression analysis revealed high similarity between the two OLM types ($R = 0.98$, $p = 2.4 \times 10^{-8}$). Next, we asked if the observed neurexin pattern in OLMs were similar to those previously identified in MGE or CGE cells. Using regression analysis, we found that the neurexin pattern in OLMs correlated with low confidence with CGE ($R = 0.53$, $p = 7.9 \times 10^{-2}$, Figure 8e), but with high confidence with MGE neurexin pattern (Lukacsovich et al., 2019; $R = 0.97$, $p = 3.3 \times 10^{-7}$, Figure 8e). Together, these splice isoform analyses are in agreement with the observation that Htr3aCre-OLM and

SstCre-OLM neurons express identical transcription factors, which indicates common developmental identity (Figure 4).

3.8 | Transcriptional differences and similarities between Htr3aCre-OLM and SstCre-OLM neurons

To analyse whether further transcriptomic differences exist between Htr3aCre-OLM and SstCre-OLM cells, we determined the complete profile of differentially expressed genes. We found that the two types were different due to a relatively low number of genes that were enriched in Htr3aCre-OLM, but not in SstCre-OLM, neurons, including *Htr3b* (Figure 9a). Next, we set out to examine to what degree these genes were able to define the two populations. First, we examined how many genes were overlapping versus non-overlapping between the two types. We did not consider genes that were not expressed in either cell type (7,960 out of 22,800), nor did we include genes with low expression in both cell types (3,620 out of 22,800). We classified a gene as being expressed or not being expressed in a cell type if it was detected in at least 40% or less than 20% of the cells in that category, respectively. To avoid ambiguous cases, we did not consider genes that could not be clearly classified as belonging or not belonging to at least one of the OLM type (4,122 out of 22,800 genes). We then looked at how many of the remaining genes (7,098 out of 22,800) were either in both or only one of the OLM types. We found that most genes (6,937 out of 7,098) were expressed in both cell types (Figure 9b). Of those genes that were present in only one OLM type, 98% (158 out of 161) were expressed in Htr3aCre-OLMs, but not in SstCre-OLMs.

To explore whether any more gradual, subtype-specific effects might be present, we generated a heatmap of the distribution of expression rates of genes across the two OLM types (Figure 9c). This plot would unambiguously display any genes that were consistently expressed in one but not in the other OLM types (such genes would have been displayed in the upper right or lower left corner in the plot). However, we found that most genes were near the unity line, with a slight shift in the general trend towards more consistent expression in Htr3aCre-OLM cells, in agreement with the pattern we found in the volcano plot (Figure 9a). Furthermore, using chi-square-based feature selection, we tested the accuracy to which OLM neurons could be classified as Htr3aCre-OLM or SstCre-OLM. We found that while the classification accuracy was consistently higher than random chance (50%), it was not higher than 70% at any gene numbers tested between 2 and 500 genes, suggesting the lack of a gene set that

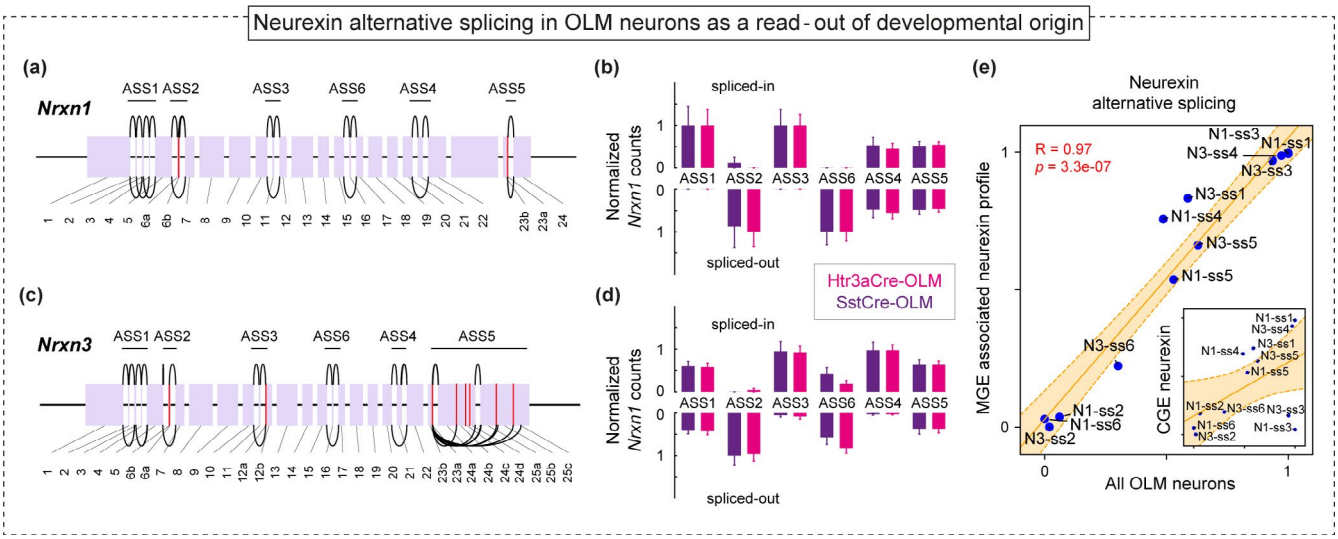

FIGURE 8 Neurexin isoform expression in OLM interneurons. (a) Exon structure of the *Nrxn1* gene. Introns are shortened for clarity, and exons (in purple, numbered in the bottom) are shown proportional to their length. Alternatively spliced exon–exon junctions are shown in black; red lines represent alternative splice donor or acceptor sites. Alternative splice sites 1–6 (ASS1-ASS6) are labelled on top. (b) Bar plots show side-by-side comparison of *Nrxn1* alternative splicing between Htr3aCre-OLM and SstCre-OLM cells. Upward bars represent exon inclusion ('spliced-in'), and downward bars represent exon exclusion ('spliced-out') in the final mRNA product. In case, for example ASS1, multiple alternatively spliced exons are present, bar plots represent total read counts. None of the paired comparisons revealed statistically significant difference (Welch's *t* test, $p > .05$). (c) Exon structure of the *Nrxn3* gene. (d) Bar plots show side-by-side comparison of *Nrxn3* alternative splicing between Htr3aCre-OLM and SstCre-OLM cells. None of the paired comparisons revealed statistically significant difference (Welch's *t* test, $p > .05$). (e) Regression analysis of *Nrxn1* and *Nrxn3* alternative splicing levels reveals strong correlation between OLM cells (where SstCre-OLM and Htr3aCre-OLM types are pooled together) and the mean MGE neurexin profiles as described in Lukacsovich et al. (2019). Insert shows regression analysis of neurexin isoforms between OLM and the mean CGE neurexin profiles

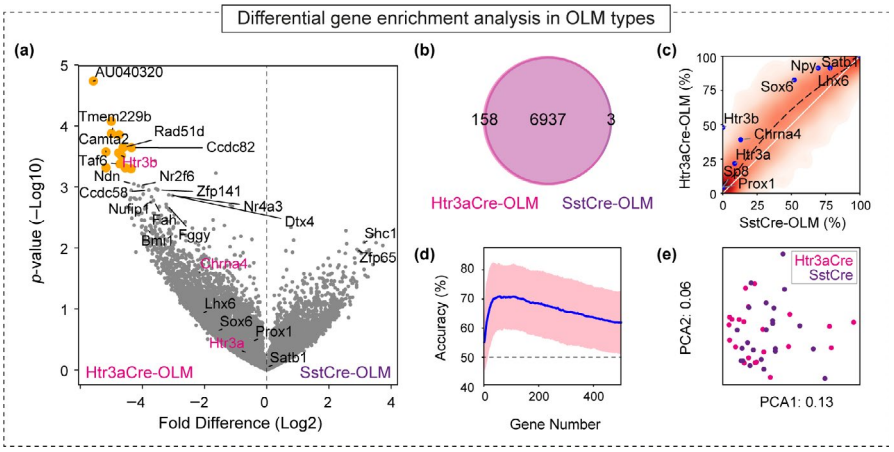

FIGURE 9 Transcriptional differences and similarities between Htr3aCre-OLM and SstCre-OLM neurons. (a) Volcano plot shows comparison of gene expression between Htr3aCre-OLM and SstCre-OLM cells. Yellow dots represent genes with at least fourfold difference expression and *p* less than .05. Genes that are enriched in Htr3a-OLM cells appear in the left, whereas genes that are enriched in Sst-OLM cells appear in the right. Labelled genes include 5-HT3 subunits, transcription-related genes, developmental origin-associated genes, as well as genes with ligase, acetase, kinase activity and unknown function (*Tmem229b*). (b) Venn diagram showing the overlap of gene expression between Htr3aCre-OLM and SstCre-OLM cells. Less than 2% of the considered genes that belong to just one population were from SstCre-OLMs. (c) Heatmap generated by a 2D Kernel density estimation (KDE), showing the expression rates of genes across the two cell types. White line: unity line; dashed line: LOWESS fit of distribution, showing a shift towards more consistent expression in Htr3aCre-OLM cells. (d) We used a bootleg method to separate our data set into a train and test set 1,000 times, and evaluated the accuracy of a linear svm on classifying OLM cells into Htr3a-OLM and Sst-OLM types using between 2 and 500 genes. For each gene number, we show the average accuracy (blue line) plus or minus the standard deviation (pink shaded region). An average accuracy of above 50% indicates the existence of differences between the two types in a higher dimensional space. (e) PCA plot based on HVG (see Methods) in Htr3aCre-OLM and SstCre-OLM cells, showing that the two populations do not separate

would unequivocally differentiate the two types (Figure 9d). Additionally, we examined whether the observed differential gene expression was sufficient to separate the two OLM types in an unbiased manner. For this, we used high-variance genes (HVG, see Methods) to perform a PCA (Figure 9e) and found the two types to be completely intermixed. Together, these analyses indicated that, while there are differentially expressed genes between the two OLM types, they are not transcriptomically distinct.

4 | DISCUSSION

OLM cells are important for fear encoding (Lovett-Barron et al., 2014; Schmid et al., 2016; Siwani et al., 2018), and 5-HT3 excitability in these cells may play a role in anxiety disorders and major depression (Krzywkowski, Davies, Feinberg-Zadek, Bräuner-Osborne, & Jensen, 2008; Martin et al., 2017; Yamada et al., 2006). Current models of hippocampal interneuron function suggest two OLM subtypes defined by 5-HT sensitivity: 5-HT3-excitable and 5-HT3-insensitive OLM cells. Because *Htr3a* expression, a gene encoding for a 5-HT3 subunit, has been presumed a marker of cells originating from the CGE neurogenic zone (Lee et al., 2010; Vucurovic et al., 2010), it has been deduced that CGE derivation might equate to 5-HT3a subunit-mediated excitability. In agreement with this notion, 5-HT3-excitable OLMs were identified using the BAC transgenic Htr3a-Cre::Ai14 and Htr3a-GFP lines (Akgül et al., 2019; Chittajallu et al., 2013). Here, we used single-cell RNA sequencing from morphologically- and electrophysiologically characterized OLM cells, generated their complete transcriptomic profiles, which confirmed previous and revealed novel observations about these cells.

Analysing the morphological and biophysical properties, we obtained a homogeneous cell population for both Htr3aCre-OLMs and SstCre-OLMs with the typical features that have been described for the OLM population (Figures 2 and 3). All cells had a fusiform cell soma residing in stratum oriens of hippocampal CA1 with horizontally spanning dendritic branches. Their axon frequently originated from a primary dendrite and projected towards the stratum lacunosum moleculare, where OLM cell axons majorly arborize. In addition, all cells displayed pronounced 'sag' potential upon hyperpolarizing current injections, spike frequency adaptation and a maximum firing frequency of <100 Hz that distinguishes them from prototypical fast-spiking interneurons (Booker & Vida, 2018; Pelkey et al., 2017). After using these properties to confirm OLM identity, we analysed the transcriptomes of these cells leading to multiple observations.

First, we found that both Htr3a-OLMs and SstCre-OLMs express *Npy* (Figure 4). Using additional immunolabelling, we confirmed the presence of the NPY peptide in OLMs

(Figure 6). This finding was unexpected, because OLM neurons in rat were found to lack immunopositivity for NPY (Katona et al., 2014, 0; /4 cells tested; Forro, Valenti, Lasztoczi, & Klausberger, 2015, 0; /3 cells tested) and a recent transcriptional survey of CA1 hippocampal interneurons consequently used this presumed lack of *Npy* expression as a criterium for OLM classification (Harris et al., 2018; note, however, that Tricoire et al. (2011) verified *Npy* mRNA expression in 1/1 OLM tested in mouse). In this manner, our single-cell RNA-Seq analysis from morphologically identified neurons helped to associate a key GABAergic marker with the OLM type in mouse.

Second, we found that Htr3a-OLMs only rarely expressed the *Htr3a* gene (Figure 4). This lack of *Htr3a* subunit expression in OLM transcriptomes was initially surprising because 5-HT3a subunits were presumed to be essential for assembly of functional 5-HT3 receptors (Davies et al., 1999). However, our results are in accordance with recent findings showing that presumed OLM neurons lacked expression of the *Htr3a* gene (Harris et al., 2018). Unlike ours, this large-scale single-cell sequencing study used the Slc32a1-Cre::R26R-tdTomato transgenic mouse line. The lack of detection of *Htr3a* in presumed OLMs could not be due to technical reasons, because this gene was consistently detected in Cck and Vip populations in their study (Figure 5). Because we used the Htr3a-Cre::Ai14 line in our analyses, it is possible that any earlier transient expression of *Htr3a* induced Cre, and thus persistent tdTomato expression, which was used to identify cells in brain slice preparations. A caveat of using this BAC transgenic line to study *Htr3a* expression is the possible scenario that *Htr3a* transgene-driven Cre, and thus tdTomato, expression differs from endogenous *Htr3a* levels. However, we found that the expression rate of *Cre* is comparable to the endogenous *Htr3a* (Figure 4) making this scenario less likely. Furthermore, we do not believe the detection of *Htr3a* is compromised in our study at steps of reverse transcription or amplification, because using similar methods, we have shown prevalent expression of *Htr3a* in regular-firing CCK interneurons in the hippocampus (Földy et al., 2016). In addition, unlike in OLMs, *Htr3a* expression appears to be stable in most CGE-derived cortical neuron types (Lukacsovich et al., 2019). Therefore, the lack of consistent *Htr3a* expression appears to be a characteristic of most OLMs.

If not the 5-HT3a subunit, then what other subunits may mediate 5-HT3 excitability? As opposed to *Htr3a*, we more frequently detected expression of the *Htr3b* gene (Figures 4 and 7). *Htr3b* appeared to be specific to the Htr3aCre-OLM population, as we did not detect this gene in any of the SstCre-OLMs. The presence of *Htr3b* could be significant, because although 5-HT3-mediated currents were readily detectable in native brain cells, homomeric 5-HT3 receptors assembled purely from 5-HT3a subunits did not display measurable single-channel conductances in heterologous expression systems (Hussy et al., 1994). In contrast, analysis of heteromeric, 5-HT3b subunit-containing 5-HT3 receptors displayed conductances in the same order of magnitude as those in native cells (Davies et al., 1999). Underlining the functional importance of 5-HT3b, a major depression-associated genetic mutation in the 5-HT3b subunit has been shown to further increase 5-HT3 receptor conductance (Krzywkowski et al., 2008). However, *Htr3b*-expressing interneurons have not been previously identified (Sudweeks et al., 2002; see also Doucet, Latrémolière, Darmon, Hamon, & Emerit, 2007). Our single-cell RNA-Seq and additional in situ hybridization analyses provide evidence for highly specific expression of *Htr3b* in Htr3aCre-OLMs, but not SstCre-OLMs. This outcome was surprising, because although the Htr3a-Cre transgenic line would seem to be useful in revealing Htr3b-expressing OLMs, given all the other transcriptomic similarities between OLMs identified in both lines, such Htr3b-expressing cells should presumably be present in the Sst-Cre line as well. In addition, none of the included *Htr3a*-expressing populations expressed *Htr3b* (Figure 5). This finding suggests that *Htr3b* expression is specific to the Htr3a-Cre transgenic line rather than to a naturally occurring subset of OLM neurons. In addition to *Htr3b*, the acetylcholine receptor 4 subunit (AChR4; encoded by the *Chrna4* gene) was also found to co-assemble with 5-HT3a's to form functional 5-HT3 receptors in hippocampal interneurons (Sudweeks et al., 2002). Using single-cell RNA-Seq, we found a more frequent expression of *Chrna4* in Htr3aCre-OLMs compared to SstCre-OLMs (Figure 4). However, additional RNAscope experiments revealed that *Chrna4* expression OLMs are present in both the Htr3a-Cre and Sst-Cre transgenic lines (Figure 7). Thus, our transcriptome analyses suggest that 5-HT3 excitability in Htr3aCre-OLMs may be mediated by either a yet un-described assembly of 5-HT3b and AChR4 subunits or co-assembly of these subunits with 5-HT3a when it is (though infrequently) present. The apparent inability of 5-HT3b to form homomeric 5-HT3 receptors in heterologous expression systems may support this scenario (Davies et al., 1999).

Third, our experiments disclosed additional information on the developmental identity of Htr3aCre-OLMs and SstCre-OLMs. Unexpectedly, Htr3aCre-OLMs consistently expressed MGE-associated *Lhx6*, *Satb1* and *Sox6* transcription factors, identically to SstCre-OLMs. Using additional gene isoform analyses, we furthermore found identical neurexin alternative splicing expression profiles between the two types. This found neurexin profile was identical to those we previously identified in $Lhx6^{+}$ interneurons of presumed MGE origin (Lukacsovich et al., 2019), supporting the notion

that Htr3aCre-OLMs and SstCre-OLMs originate from a common neurogenic zone, which may be the MGE (Figures 4 and 8).

In the embryonic telencephalon, CGE and MGE are well-studied neurogenic zones, which generate distinct types of interneurons. $Pvalb^+$ and Sst^+ interneurons have been shown to derive from the MGE (Fogarty et al., 2007; Kessaris et al., 2014), whereas Cck^+, Vip^+ and $Reln^+$ interneurons derive from the CGE (Lee et al., 2010; Vucurovic et al., 2010). In addition, the preoptic area (POA) has emerged as another neurogenic zone, presumed to generate ~10% of cortical interneurons (Gelman et al., 2009, 2011; Niquille et al., 2018). While defining differences between POA- versus MGE- and CGE-derived types remains an important question, progenitor cells in the POA have been shown to co-express *Nkx2.1* and *Htr3a* (Niquille et al., 2018), which were previously associated with MGE or CGE origin, respectively. In the light of this, it is possible that OLMs might also derive from the POA. While our transcriptomic analysis argues that OLMs have shared neurogenic origin, a completely definitive determination of their origin would require lineage tracing from their progenitor pool.

Finally, whole-transcriptome differential gene expression analysis revealed a bias of more genes being expressed in Htr3aCre-OLMs compared to SstCre-OLMs. However, the number of differentially expressed genes was relatively limited and could not unambiguously differentiate the two types (Figure 9). The differentially expressed genes may suggest the presence of ongoing transcriptional activity in Htr3aCre-OLMs, which potentially also includes dynamic regulation of *Htr3a*, or may disclose added consequences of the genomic integration of the BAC insert.

In summary, we found consistent expression of *Npy* in OLM neurons, both on a transcriptional and peptide level. Additionally, our results reveal high expression of the 5-HT3 receptor-coding subunit *Htr3b* in Htr3aCre-OLMs, but not in SstCre-OLMs. Furthermore, we found that all OLMs express *Sst*, but only some express *Htr3a*, suggesting that *Htr3a*-expressing OLMs comprise a subpopulation of all OLM neurons, a property of which may be defined at progenitor stage and is independent of the developmental origin. Alternatively, *Htr3a* expression may be acquired during circuit maturation (Lim, Mi, Llorca, & Marín, 2018; Wamsley & Fishell, 2017) or may take place at any later time point. While this remains an important question, our findings highlight a higher homogeneity among the OLM population than previously envisioned and provide evidence only for one common neurogenic identity in OLM neurons. These findings uncover new insights in GABAergic cell diversity and OLM identity at a transcriptomic level, and important next steps would be to study at both the isoform and the proteomic level to validate transcriptomic patterns.

ACKNOWLEDGEMENT

This work was supported by grants from the Swiss National Science Foundation (CRETP3_166815 and 31003A_170085 to C.F.). We thank Drs J. Szabadics and T. Lukacsovich for discussions, members of the Functional Genomic Center Zurich for their support with sequencing, and Dr H. Rehrauer for his valuable support with bioinformatics pipelines.

CONFLICT OF INTEREST

The authors declare no conflict of interest.

DATA AVAILABILITY STATEMENT

Raw sequences are deposited and freely available under NCBI GEO # GSE124847.

AUTHOR CONTRIBUTIONS

JW and LQ performed electrophysiological recordings; DL analysed electrophysiological and transcriptomic data; JW reconstructed neuron morphology; JW and LQ performed single-cell RNA-Seq; AS, WL, JW and LQ performed in situ hybridization experiments; JW, LQ, DL and CF wrote the manuscript.

ORCID

Csaba Földy https://orcid.org/0000-0001-8709-8490

REFERENCES

Akgül, G., Abebe, D., Yuan, X. Q., Auville, K., & McBain, C. J. (2019). The role of AMPARs in the maturation and integration of caudal ganglionic eminence-derived interneurons into developing hippocampal microcircuits. *Scientific Reports*, *9*(1), 5435.

Batista-Brito, R., Rossignol, E., Hjerling-Leffler, J., Denaxa, M., Wegner, M., Lefebvre, V., … Fishell, G. (2009). The cell-intrinsic requirement of Sox6 for cortical interneuron development. *Neuron*, *63*(4), 466–481.

Baude, A., Nusser, Z., Roberts, J. D. B., Mulvihill, E., Mcllhinney, R. A. J., & Somogyi, P. (1993). The metabotropic glutamate receptor (mGluRlα) is concentrated at perisynaptic membrane of neuronal subpopulations as detected by immunogold reaction. *Neuron*, *11*, 771–787.

Böhm, C., Pangalos, M., Schmitz, D., & Winterer, J. (2015). Serotonin attenuates feedback excitation onto O-LM interneurons. *Cerebral Cortex*, *25*(11), 4572–4583.

Booker, S. A., & Vida, I. (2018). Morphological diversity and connectivity of hippocampal interneurons. *Cell and Tissue Research*, *373*, 619–641.

Chen, C., Arai, I., Satterfield, R., Young, S. M. Jr, & Jonas, P. (2017). Synaptotagmin 2 is the fast Ca2+ sensor at a central inhibitory synapse. *Cell Reports*, *18*(3), 723–736.

Chittajallu, R., Craig, M. T., McFarland, A., Yuan, X., Gerfen, S., Tricoire, L., … McBain, C. J. (2013). Dual origins of functionally distinct O-LM interneurons revealed by differential 5-HT(3A)R expression. *Nature Neuroscience*, *16*(11), 1598–1607.

Close, J., Xu, H., De Marco García, N., Batista-Brito, R., Rossignol, E., Rudy, B., & Fishell, G. (2012). Satb1 is an activity-modulated transcription factor required for the terminal differentiation and connectivity of medial ganglionic eminence-derived cortical interneurons. *Journal of Neuroscience*, *32*(49), 17690–17705.

Davies, P. A., Pistis, M., Hanna, M. C., Peters, J. A., Lambert, J. J., Hales, T. G., & Kirkness, E. F. (1999). The 5-HT3B subunit is a major determinant of serotonin-receptor function. *Nature*, *397*(6717), 359–363.

Denaxa, M., Kalaitzidou, M., Garefalaki, A., Achimastou, A., Lasrado, R., Maes, T., & Pachnis, V. (2012). Maturation-promoting activity of SATB1 in MGE-derived cortical interneurons. *Cell Reports*, *2*, 1351–1362.

Doucet, E., Latrémolière, A., Darmon, M., Hamon, M., & Emerit, M. B. (2007). Immunolabelling of the 5-HT 3B receptor subunit in the central and peripheral nervous systems in rodents. *European Journal of Neuroscience*, *26*(2), 355–366.

Fogarty, M., Grist, M., Gelman, D., Marín, O., Pachnis, V., & Kessaris, N. (2007). Spatial genetic patterning of the embryonic neuroepithelium generates GABAergic interneuron diversity in the adult cortex. *Journal of Neuroscience*, *27*(41), 10935–10946.

Földy, C., Darmanis, S., Aoto, J., Malenka, R. C., Quake, S. R., & Südhof, T. C. (2016). Single-cell RNAseq reveals cell-adhesion profiles in electrophysiologically defined neurons. *PNAS*, *113*(35), E5222–E5231.

Forro, T., Valenti, O., Lasztoczi, B., & Klausberger, T. (2015). Temporal organization of GABAergic interneurons in the intermediate CA1 hippocampus during network oscillations. *Cerebral Cortex*, *25*(5), 1228–1240.

Gelman, D., Griveau, A., Dehorter, N., Teissier, A., Varela, C., Pla, R., … Marín, O. (2011). A wide diversity of cortical GABAergic interneurons derives from the embryonic preoptic area. *Journal of Neuroscience*, *31*(46), 16570–16580.

Gelman, D. M., Martini, F. J., Nóbrega-Pereira, S., Pierani, A., Kessaris, N., & Marín, O. (2009). The embryonic preoptic area is a novel source of cortical GABAergic interneurons. *Journal of Neuroscience*, *29*(29), 9380–9389.

Gerfen, C. R., Paletzki, R., & Heintz, N. (2013). GENSAT BAC cre-recombinase driver lines to study the functional organization of cerebral cortical and basal ganglia circuits. *Neuron*, *80*(6), 1368–1383.

Gloveli, T., Dugladze, T., Saha, S., Monyer, H., Heinemann, U., Traub, R. D., … Buhl, E. H. (2005). Differential involvement of oriens/pyramidale interneurones in hippocampal network oscillations in vitro. *Journal of Physiology*, *562*(Pt 1), 131–147.

Harris, K. D., Hochgerner, H., Skene, N. G., Magno, L., Katona, L., Bengtsson Gonzales, C., … Hjerling-Leffler, J. (2018). Classes and continua of hippocampal CA1 inhibitory neurons revealed by single-cell transcriptomics. *PLoS Biology*, *16*(6), e2006387.

Hussy, N., Lukas, W., & Jones, K. A. (1994). Functional properties of a cloned 5-hydroxytryptamine ionotropic receptor subunit: Comparison with native mouse receptors. *Journal of Physiology*, *481*(Pt 2), 311–323.

Katona, L., Lapray, D., Viney, T. J., Oulhaj, A., Borhegyi, Z., Micklem, B. R., … Somogyi, P. (2014). Sleep and movement differentiates actions of two types of somatostatin-expressing GABAergic interneurons in rat hippocampus. *Neuron*, *82*, 872–886.

Kelley, S. P., Dunlop, J. I., Kirkness, E. F., Lambert, J. J., & Peters, J. A. (2003). A cytoplasmic region determines single-channel conductance in 5-HT3 receptors. *Nature*, *424*(6946), 321–324.

Kessaris, N., Magno, L., Rubin, A. N., & Oliveira, M. G. (2014). Genetic programs controlling cortical interneuron fate. *Current Opinion in Neurobiology*, *26*, 79–87.

Klausberger, T., & Somogyi, P. (2008). Neuronal diversity and temporal dynamics: The unity of hippocampal circuit operations. *Science*, *321*(5885), 53–57.

Kondo, M., Nakamura, Y., Ishida, Y., Yamada, T., & Shimada, S. (2013). The 5-HT3A receptor is essential for fear extinction. *Learning & Memory*, *21*(1), 1–4.

Krzywkowski, K., Davies, P. A., Feinberg-Zadek, P. L., Bräuner-Osborne, H., & Jensen, A. A. (2008). High-frequency HTR3B variant associated with major depression dramatically augments the signaling of the human 5-HT3AB receptor. *Proceedings of the National Academy of Sciences of the United States of America*, *105*(2), 722–727.

Lamsa, K. P., Heeroma, J. H., Somogyi, P., Rusakov, D. A., & Kullmann, D. M. (2007). Anti-hebbian long-term potentiation in the hippocampal feedback inhibitory circuit. *Science*, *315*(5816), 1262–1266.

Leão, R. N., Mikulovic, S., Leão, K. E., Munguba, H., Gezelius, H., Enjin, A., … Kullander, K. (2012). OLM interneurons differentially modulate CA3 and entorhinal inputs to hippocampal CA1 neurons. *Nature Neuroscience*, *15*(11), 1524–1530.

Lee, S. H., Hjerling-Leffler, J., Zagha, E., Fishell, G., & Rudy, B. (2010). The largest group of superficial neocortical GABAergic interneurons expresses ionotropic serotonin receptors. *Journal of Neuroscience*, *30*(50), 16796–16808.

Lein, E. S., Hawrylycz, M. J., Ao, N., Ayres, M., Bensinger, A., Bernard, A., … Jones, A. R. (2007). Genome-wide atlas of gene expression in the adult mouse brain. *Nature*, *445*, 168–176.

Lien, C. C., Martina, M., Schultz, J. H., Ehmke, H., & Jonas, P. (2002). Gating, modulation and subunit composition of voltage-gated K(+) channels in dendritic inhibitory interneurones of rat hippocampus. *Journal of Physiology*, *538*(Pt 2), 405–419.

Lim, L., Mi, D., Llorca, A., & Marín, O. (2018). Development and functional diversification of cortical interneurons. *Neuron*, *100*(2), 294–313.

Liodis, P., Denaxa, M., Grigoriou, M., Akufo-Addo, C., Yanagawa, Y., & Pachnis, V. (2007). Lhx6 activity is required for the normal migration and specification of cortical interneuron subtypes. *Journal of Neuroscience*, *27*(12), 3078–3089.

Lovett-Barron, M., Kaifosh, P., Kheirbek, M. A., Danielson, N., Zaremba, J. D., Reardon, T. R., … Losonczy, A. (2014). Dendritic inhibition in the hippocampus supports fear learning. *Science*, *343*(6173), 857–863.

Lukacsovich, D., Winterer, J., Que, L., Wenshu, L., Lukacsovich, T., & Földy, C. (2019). Single-cell RNAseq reveals developmental origins and ontogenetic stability of neurexin alternative splicing profiles. *Cell Reports*, *27*(13), 3752–3759.

Lun, A. T. L., McCarthy, D. J., & Marioni, J. C. (2016). A step-by-step workflow for low-level analysis of single-cell RNA-seq data with bioconductor. *F1000Res*, *5*, 2122.

Luo, X., Muñoz-Pino, E., Francavilla, R., Vallée, M., Droit, A., & Topolnik, L. (2019). Transcriptomic profile of the subiculum-projecting VIP GABAergic neurons in the mouse CA1 hippocampus. *Brain Structure and Function*, *224*(6), 2269–2280.

Maccaferri, G. (2005). Stratum oriens horizontal interneurone diversity and hippocampal network dynamics. *Journal of Physiology*, *562*(Pt 1), 73–80.

Magnin, E., Francavilla, R., Amalyan, S., Gervais, E., David, L. S., Luo, X., & Topolnik, L. (2019). Input-specific synaptic location and function of the α5 GABAA receptor subunit in the mouse CA1 hippocampal neurons. *Journal of Neuroscience*, *39*(5), 788–801.

Maricq, A. V., Peterson, A. S., Brake, A. J., Myers, R. M., & Julius, D. (1991). Primary structure and functional expression of the 5HT3 receptor, a serotonin-gated ion channel. *Science*, *254*(5030), 432–437.

Martin, V., Riffaud, A., Marday, T., Brouillard, C., Franc, B., Tassin, J. P., … Lanfumey, L. (2017). Response of Htr3a knockout mice to antidepressant treatment and chronic stress. *British Journal of Pharmacology*, *174*(15), 2471–2483.

Miyoshi, G., Young, A., Petros, T., Karayannis, T., McKenzie Chang, M., Lavado, A., … Fishell, G. (2015). Prox1 regulates the subtype-specific development of caudal ganglionic eminence-derived GABAergic cortical interneurons. *Journal of Neuroscience*, *35*(37), 12869–12889.

Niquille, M., Limoni, G., Markopoulos, F., Cadilhac, C., Prados, J., Holtmaat, A., & Dayer, A. (2018). Neurogliaform cortical interneurons derive from cells in the preoptic area. *Elife*, *7*, e32017.

Pangalos, M., Donoso, J. R., Winterer, J., Zivkovic, A. R., Kempter, R., Maier, N., & Schmitz, D. (2013). Recruitment of oriens-lacunosum-moleculare interneurons during hippocampal ripples. *PNAS*, *110*(11), 4398–4403.

Paul, A., Crow, M., Raudales, R., He, M., Gillis, J., & Huang, Z. J. (2017). Transcriptional architecture of synaptic communication delineates GABAergic neuron identity. *Cell*, *171*(3), 522–539.

Pelkey, K. A., Chittajallu, R., Craig, M. T., Tricoire, L., Wester, J. C., & McBain, C. J. (2017). Hippocampal GABAergic inhibitory interneurons. *Physiological Reviews*, *97*(4), 1619–1747.

Que, L., Winterer, J., & Földy, C. (2019). Deep survey of GABAergic interneurons: emerging insights from gene-isoform transcriptomics. *Frontiers in Molecular Neuroscience*, *12*, 115.

Royer, S., Zemelman, B. V., Losonczy, A., Kim, J., Chance, F., Magee, J. C., & Buzsáki, G. (2012). Control of timing, rate and bursts of hippocampal place cells by dendritic and somatic inhibition. *Nature Neuroscience*, *15*(5), 769–775.

Salesse, C., Mueller, C. L., Chamberland, S., & Topolnik, L. (2011). Age-dependent remodelling of inhibitory synapses onto hippocampal CA1 oriens-lacunosum moleculare interneurons. *Journal of Physiology*, *589*(Pt 20), 4885–4901.

Schmid, L. C., Mittag, M., Poll, S., Steffen, J., Wagner, J., Geis, H. R., … Fuhrmann, M. (2016). Dysfunction of somatostatin-positive interneurons associated with memory deficits in an Alzheimer's disease model. *Neuron*, *92*(1), 114–125.

Schreiner, D., Nguyen, T. M., Russo, G., Heber, S., Patrignani, A., Ahrné, E., & Scheiffele, P. (2014). Targeted combinatorial alternative splicing generates brain region-specific repertoires of neurexins. *Neuron*, *84*(2), 386–398.

Siwani, S., França, A. S. C., Mikulovic, S., Reis, A., Hilscher, M. M., Edwards, S. J., … Kullander, K. (2018). OLMα2 cells bidirectionally modulate learning. *Neuron*, *99*(2), 404–412.

Südhof, T. C. (2017). Synaptic neurexin complexes: A molecular code for the logic of neural circuits. *Cell*, *171*(4), 745–769.

Sudweeks, S. N., Hooft, J. A., & Yakel, J. L. (2002). Serotonin 5-HT(3) receptors in rat CA1 hippocampal interneurons: Functional and molecular characterization. *Journal of Physiology*, *544*(3), 715–726.

Sylwestrak, E. L., & Ghosh, A. (2012). Elfn1 regulates target-specific release probability at CA1-interneuron synapses. *Science*, *338*(6106), 536–540.

Topolnik, L., Chamberland, S., Pelletier, J. G., Ran, I., & Lacaille, J. C. (2009). Activity-dependent compartmentalized regulation of dendritic Ca2 + signaling in hippocampal interneurons. *Journal of Neuroscience*, *29*(14), 4658–4663.

Treutlein, B., Gokce, O., Quake, S. R., & Südhof, T. C. (2014). Cartography of neurexin alternative splicing mapped by single-molecule long-read mRNA sequencing. *PNAS*, *111*(13), E1291–E1299.

Tricoire, L., Pelkey, K. A., Erkkila, B. E., Jeffries, B. W., Yuan, X., & McBain, C. J. (2011). A blueprint for the spatiotemporal origins of mouse hippocampal interneuron diversity. *Journal of Neuroscience*, *31*(30), 10948–10970.

Tripathy, S. J., Toker, L., Bomkamp, C., Mancarci, B. O., Belmadani, M., & Pavlidis, P. (2018). Assessing transcriptome quality in patch-seq datasets. *Frontiers in Molecular Neuroscience*, *11*, 363.

Vucurovic, K., Gallopin, T., Ferezou, I., Rancillac, A., Chameau, P., van Hooft, J. A., … Vitalis, T. (2010). Serotonin 3A receptor subtype as an early and protracted marker of cortical interneuron subpopulations. *Cerebral Cortex*, *20*(10), 2333–2347.

Wamsley, B., & Fishell, G. (2017). Genetic and activity-dependent mechanisms underlying interneuron diversity. *Nature Reviews Neuroscience*, *18*(5), 299–309.

Yamada, K., Hattori, E., Iwayama, Y., Ohnishi, T., Ohba, H., Toyota, T., … Yoshikawa, T. (2006). Distinguishable haplotype blocks in the HTR3A and HTR3B region in the Japanese reveal evidence of association of HTR3B with female major depression. *Biological Psychiatry*, *60*(2), 192–201.

How to cite this article: Winterer J, Lukacsovich D, Que L, Sartori AM, Luo W, Földy C. Single-cell RNA-Seq characterization of anatomically identified OLM interneurons in different transgenic mouse lines. *Eur J Neurosci*. 2019;50:3750–3771. https://doi.org/10.1111/ejn.14549